



## Multiscale estimation of the field-aligned current density

Costel Bunescu<sup>1,2</sup>, Joachim Vogt<sup>2</sup>, Adrian Blagau<sup>1</sup>, and Octav Marghitu<sup>1</sup>

<sup>1</sup>Institute of Space Science, Bucharest, Romania.

<sup>2</sup>Department of Physics and Earth Science, Jacobs University Bremen, Bremen, Germany.

**Correspondence:** C. Bunescu ([costel@spacescience.ro](mailto:costel@spacescience.ro))

**Abstract.** Field-aligned currents (FACs) in the magnetosphere-ionosphere (M-I) system exhibit a range of spatial and temporal scales that are linked to key dynamic coupling processes. To disentangle the scale dependence in magnetic field signatures of auroral FACs and to characterize their geometry and orientation, Bunescu et al. (2015) introduced the multi-scale FAC analyzer framework based on minimum variance analysis (MVA) of magnetic time series segments. In the present report this approach is carried further to include in the analysis framework a FAC density scalogram, i.e., a multiscale representation of the FAC density time series. The new technique is validated and illustrated using synthetic data consisting of overlapping sheets of FACs at different scales. The method is applied to Swarm data showing both large-scale and quiet aurora as well as mesoscale FAC structures observed during more disturbed conditions. We show both planar and non-planar FAC structures as well as uniform and non-uniform FAC density structures. For both, synthetic and Swarm data, the multiscale analysis is applied by two scale sampling schemes, namely the linear, and the logarithmic scanning of the FACs scale domain. The scale integrated FAC density is computed by both small-scale and large-scale weighting. The integrated multiscale FAC density is compared with the input FAC density for the synthetic data, whereas for the Swarm data we cross-check the results with well established single- and dual-spacecraft techniques. The entire multiscale information provides a new visualization tool for the complex FAC signatures, that complement other FAC analysis tools.

### 1 Introduction

The dynamics of the magnetosphere-ionosphere (M-I) system at auroral latitudes is essentially controlled by solar wind-magnetosphere (S-M) coupling. One result of the dynamic interaction in the global S-M system is the accumulation of magnetic flux in different parts of the system, e.g., the magnetotail. The energy in the large-scale components is transported and dissipated to smaller scale components of the system, e.g., the polar ionosphere. The transfer of energy and momentum in the system is mediated by field-aligned currents (FACs) flowing along the ambient magnetic field lines, and driving the formation of ionospheric (Hall and Pedersen) currents. The entire chain of the energy flow and conversion mechanisms is governed by a multiscale behavior both in time and in space. The multiscale character is observed in all the measurable quantities associated to the system, like magnetic field measurements from above (spacecraft) and below (ground) the ionosphere. While above the ionospheres one measures the FACs perturbation, related mainly to the ionospheric Pedersen currents, on ground one measures mainly the Hall currents influence. The multiscale character is observed as well in the measurements of optical emissions, associated in turn to a multiscale particle precipitation pattern.



The spatial and temporal scales of the auroral arcs observed optically on ground are dependent on the characteristics of the optical instruments (e.g. resolution, sampling frequency, coverage, exposure). Earlier statistical measurements of the auroral arc thickness (Maggs and Davis, 1968) were based on narrow field of view (FoV) TV camera observations and found a median of the scale distribution around 230 m in the range of fine and small scale auroral arcs (10 m-1 km). Later measurements (Knudsen et al., 2001) based on All-Sky-Imager (ASI) observations found a maximum of the scale distribution around 18 km in the range of mesoscale arcs (10-100 km). The TV and ASI observations are also responding to different temporal scales because of the large sampling frequency difference, maximum at about  $\sim 25$  Hz for TV and  $\sim 0.3$  Hz for ASI. More recently, Partamies et al. (2010), showed measurements based on intermediate FoV optics (FoV of  $20^\circ$  and spatial resolution of 100 m) with a median of the arc widths distribution around 0.5-1.5 km. Partamies et al. (2010) observations fit in between the previous fine and mesoscale arc width distributions. While these studies concentrated on the visible arcs, Trondsen and Cogger (1997) addressed the scale distribution of the black aurora and found a maximum around 400-500 m with the average width of 615 m (range between 200 m and 1 km). Overall, the results of all these studies indicates a rather continuous scale spectrum (Partamies et al., 2010).

FAC structures in the auroral zone are typically organized in east-west aligned sheets. The first statistical studies (Iijima and Potemra, 1976a, b) of the large scale FACs separated those into the well known poleward (R1) and equatorward (R2) currents with different orientation depending on the magnetic local time (MLT) sector. More recent studies e.g. (He et al., 2012) refined this picture and modeled the FACs properties (e.g. thickness and intensity) as a function of the solar wind properties and geomagnetic indices (e.g. AE index). The internal structure of large-scale FACs, associated to e.g. discrete auroral arcs, shows variability in all observed characteristics (e.g. the spatial and temporal scales, orientation, geometry) depending on MLT and substorm phase.

Above the ionosphere, spacecraft observations provide information about the scale distribution and main characteristics of the FACs through the measurements of magnetic fields (upward and downward FACs), associated electric fields (monopolar, converging or diverging bipolar), and particle fluxes (upgoing and downgoing). Karlsson and Marklund (1996) found a median scale of about 4.6 km for the diverging electric fields observed by Freja. A relatively close scale distribution with a maximum between 4-5 km was obtained by Johansson et al. (2007) using Cluster measurements (3-6  $R_E$  altitude) of intense electric fields ( $>0.15$  V/m). Johansson et al. (2007) found that the associated FACs and density gradients have also typical values within 4-5 km range. A statistical study of inverted V structures (U shaped potential drops) observed by the FAST satellite (Partamies et al., 2008) showed typical scale widths of 20-40 km (maximum energies of 2-4 keV). Simultaneous measurements of narrow arc structures (down to a few km) both in particle and optical data were shown by Stenbaek-Nielsen et al. (1998) by analyzing conjugate FAST/aircraft observations. In the small-scale range observation we mention also the high resolution measurements of fine scale FACs observed by Freja (Lühr et al., 1994) showing a minimum FAC scales of  $\sim 1.7$  km.

The scale distribution of FACs reflects a variety of the M-I coupling mechanisms. At large scales we have a quasi-stationary coupling (FACs closing in the ionosphere), whereas at small and fine scales a time dependent coupling, typically provided by Alfvén waves in different regimes (e.g. shear, kinetic, inertial). The interaction of shear Alfvén waves with the auroral acceleration region (Vogt and Haerendel, 1998; Vogt, 2002) presents a maximum absorption (conversion of Poynting flux to



electron energy flux) for wavelengths that are consistent with the scale size of mesoscale auroral arcs. The arc generation through inertial Alfvén waves (Chaston et al., 2003) shows scales corresponding to fine scale auroral arcs (1 km width) near the polar cap boundary.

Multi-spacecraft missions on low-altitude polar orbits (e.g. Swarm, ST5) offer a high coverage of the auroral oval and enable statistical studies that address the dynamics and stationarity of FACs, more precise FAC estimates, as well as comparison with the currents inferred by ground magnetic field measurements or cross-check with optical observations. Forsyth et al. (2017) computed the stability of FACs by comparing the lower altitude Swarm satellites (SwA, SwC) FAC density using a shape and an amplitude correlation and found that  $\sim 50\%$  and  $\sim 1-5\%$  of the large- and small-scale FACs, respectively, correlate between the two spacecraft. Previous correlation analysis using SwA/SwC (Lühr et al., 2015) addressed the stationarity and the planar geometry assumption and found small and large-scale FACs stationary on 10 s and 60 s, respectively. Comparison of Swarm FAC density with ground data was done by Juusola et al. (2016). Statistical analysis of the magnetic field perturbation ( $\Delta B$ ) measured by ST-5 spacecraft (Gjerloev et al., 2011) showed  $\Delta B$  dependence on time and scale as well as on the geomagnetic conditions and local time. For small and mesoscale structures the statistical lifetime of the structures varies linearly with the structure width. The same is true for large-scales, however in this case the rate of variation is significantly higher. The minimum relevant scale size identified by Gjerloev et al. (2011) is about 20 km and thus in the mesoscale range (Knudsen et al., 2001).

Due to the known statistical alignment of the large- and mesoscale FACs with MLT, single-spacecraft methods typically do not consider the orientation of the FACs in the plane perpendicular to  $B$ . The assumption of east-west alignment was verified by Gillies et al. (2014) in a statistical study of optical observations based on the THEMIS ASI array. Gillies et al. (2014) survey addressed the stable presubstorm auroral arcs to infer their multiplicity and orientation with respect to the magnetic east-west direction. Their results show the prevalence of multiple arc systems with respect to single arcs. Essentially the quiet arcs show east-west alignment around 23 MLT and inclination within a few degrees toward north and south at later and earlier times, respectively. The dependence of the tilt angle on MLT is linear, with a variation of about  $1^\circ$  per MLT hour. A similar analysis of the arc orientation was performed by Wu et al. (2017) who found tilts  $< 10^\circ$ . Correction of the FAC density with orientation was done by Gillies et al. (2015) using the high resolution Swarm measurements. Due to the small deviations of the arc orientation from the east-west direction they obtained just small corrections when including the orientation. During more disturbed times one expect to have a higher variation in the arc orientation. We are not aware of statistical studies addressing the orientation in various substorm phases and at small-scales. In order to obtain more accurate estimates of the FAC density, particularly for the small-scales and locally planar embedded FACs, one has to correct the FAC density by using the orientation information.

With a few exceptions, most of the FAC studies based on Swarm use mainly the low resolution (1 s) data, associated to a mapped scale of  $\sim 7.6$  km, whereas the full resolution measurements (0.02 s) correspond to  $\sim 150$  m. Small scale FACs play an important role in different stages of the aurora and a proper multiscale analysis of the FAC density is important. High resolution Swarm data conjugate with THEMIS ASI measurements were used by (Gillies et al., 2015) for the study of small-scale pulsating aurora patches. While their findings are related to pulsating aurora, e.g. strong downward currents at the



edges of the pulsating form and typically weaker upward currents inside the patches, Gillies et al. (2015) pointed out that the single-spacecraft FAC density provides better identification of the boundaries of the auroral patches.

To study the multiscale nature of auroral FACs in sufficient rigour and detail, the arsenal of space physics analysis tools ought to be amended with proper multiscale versions of classical methods. The multiscale FAC analyzer (Bunescu et al., 2015), denoted MSMVA, extends minimum variance analysis (MVA) (Sonnerup and Cahill, 1967; Sonnerup and Scheible, 1998) by providing continuous and multiscale information on the planarity and orientation of the FACs. MSMVA allows to identify the location and characteristic scale of the planar FACs. MSMVA was used (Bunescu et al., 2017) to correlate conjugate observations of FACs by FAST and Cluster spacecraft.

This paper extends the MSMVA framework (Bunescu et al., 2015) with the addition of a FAC density scalogram, i.e., a multiscale representation of the FAC density that takes into account the orientation derived from MSMVA. The extended MSMVA framework forms a consistent visualization tool, useful for the analysis of complex FAC systems in terms of their scales. Two different scale sampling schemes are considered and tested using synthetic data and Swarm measurements. The FAC density time series is reconstructed through weighted averaging of the scalogram coefficients. The results of three weighting schemes are compared with single-spacecraft and dual-spacecraft FAC density estimates (Ritter et al., 2013; Ritter and Lühr, 2006; Vogt et al., 2009, 2013).

The article is organized as follows. Section 2 reviews the MSMVA and describes the multiscale current density. In section 3 the method is applied to the magnetic signatures of synthetic currents showing both large and superposed smaller scale structures. Section 4 shows applications to Swarm events with both quiet and more dynamic and smaller scale FAC features. A discussion is presented in section 5 and the paper is concluded in section 6.

## 2 MSMVA estimation of the FAC density

Statistical studies of FACs are typically carried out in global geocentric coordinates systems such as GEO. Individual crossings are often studied in mean-field aligned (MFA) systems which are local, centered in the spacecraft, and with the third ( $z$ ) axis pointing along the background magnetic field  $B$ . Then the  $y$  and  $x$  axis point roughly to the east ( $B \times R$  where  $R$  is the radial vector to the spacecraft) and to the north, respectively.

In this paper we distinguish between general MFA frames (coordinates  $x, y, z$ ) and reference systems of FAC sheets with coordinates  $\xi, \eta, \zeta$ . Here  $\xi$  is along the sheet normal,  $\eta$  is tangential to the sheet, and  $\zeta$  points along the ambient magnetic field. The magnetic field perturbation  $\Delta B$  (oriented along  $\eta$  at an idealized infinite planar sheet) caused by the FAC sheet is obtained after subtraction of an average or model magnetic field from the magnetic vector measurements  $B$  (section 4.1).

### 2.1 Principles of single-spacecraft FAC estimation

FAC density estimators can be based on single-spacecraft or multi-spacecraft data (Ritter et al., 2013; Vogt et al., 2013). Here we adopt the single-spacecraft approach to construct a FAC density scalogram, i.e., a multiscale representation of FAC density.



Single-spacecraft FAC estimators are based on Ampère's law,  $j = \mu_0^{-1} \nabla \times \mathbf{B}$ , with the field-aligned component given by

$$j_{\parallel} = j_z = \mu_0^{-1} (\partial_x B_y - \partial_y B_x) \quad (1)$$

For a sufficiently elongated FAC sheet with coordinates  $\zeta$  and  $\xi$  pointing along the ambient magnetic field and the sheet normal, respectively, and  $\hat{\eta} = \hat{\zeta} \times \hat{\xi}$ , Equation 1 reduces to

$$j_{\parallel} = j_{\zeta} \simeq \mu_0^{-1} \partial_{\xi} B_{\eta} \quad (2)$$

The typical method used to describe the orientation of the FACs is the MVA (Sonnerup and Scheible, 1998) applied to the magnetic field measurements. MVA is based on the assumption of planarity and stationarity. MVA analysis for FACs can be performed on all components of  $\mathbf{B}$  (3D MVA) or, in a simplified case, on the perpendicular perturbation,  $\mathbf{B}_{\perp}$  (2D MVA). The full 3D MVA can be applied in any reference frame, e.g. GEO, MFA and yields  $\lambda_{\min}$ ,  $\lambda_{\text{int}}$ , and  $\lambda_{\max}$  associated to the directions along  $\mathbf{B}$ , perpendicular and tangential to the arc, respectively. The 2D MVA provides only  $\lambda_{\min} \equiv \lambda_{\xi}$  and  $\lambda_{\max} \equiv \lambda_{\eta}$  associated to the normal and tangential directions to the arc, and is rather limited to MFA frames. The GEO frame requires the 3D MVA since we do not have a strict alignment of the  $z$  axis with  $\mathbf{B}$  and part of the variance of  $\Delta \mathbf{B}$  is contained in the parallel component. We note that various other combinations are also possible by imposing constraints on  $e_{\min}$ , e.g. aligned with  $\mathbf{B}$ . In the following we use the subscripts min, int, and max when referring to the 3D MVA and  $\xi$ ,  $\eta$  for the 2D MVA.

The analysis performed in this paper is done in the MFA coordinates and takes into account only the variance in  $\mathbf{B}_{\perp}$ . By using this simplified approach we get a lower variance in the data (not including  $\mathbf{B}_{\parallel}$ ) and thus expect better results with respect to the 3D case. The 2D approach is particularly useful for the case of small scale FACs in order to avoid ambiguous cases where  $e_{\min}$  is associated to a perpendicular direction rather than to  $\mathbf{B}_{\parallel}$  direction. Moreover, we note that at the low altitude Swarm orbit  $B_z$  (or  $B_{\zeta}$ ) can be affected by large scale remote current systems in the ionosphere, e.g. the electrojet current. A statistical study emphasizing the global characteristics of the Hall current derived from Swarm observations was shown by Huang et al. (2017).

## 2.2 Reference FAC density profiles from single- and multi-spacecraft data

In the idealized case of an infinite planar current sheet oriented along the east-west direction (east-west aligned auroral arcs), the FAC density is approximated by discretizing equation (1) and by using the spacecraft velocity to compute the spatial gradient along the normal to the FAC structure:

$$j_{\parallel} = (\mu_0 v_{\perp})^{-1} \Delta B_y / \Delta t \quad (3)$$

For the quasi-static FAC approximation and in the case of spacecraft crossing along the normal to the arc, equation (3) gives correct results. In reality, due to the orbital configuration and FAC dynamics, the crossings are not normal to the arc and the FACs show deviations from the quasi-static approximation. Equation (3) was used to obtain partial estimates of the FAC density for many single-spacecraft missions, e.g. Freja (Luhr et al., 1996).



For an east-west aligned FAC sheet, the observed sign of the slope in the  $B_y$  time series (with the  $y$  axis pointing towards east) depends not only on the FAC direction but also on the direction of the spacecraft velocity  $\mathbf{V}$  and on the hemisphere. The sign of  $B_y$  time series slope equals FAC direction w.r.t.  $\mathbf{B}_0$  for poleward motion, whereas this relation is reversed for equatorward motion. The general algebraic relationship for a sheet with normal unit vector  $\hat{\mathbf{n}}$  is

$$5 \quad \mu_0 \mathbf{j} = \frac{\hat{\mathbf{n}} \times \dot{\mathbf{B}}}{V_n} = \frac{\hat{\mathbf{n}} \times \dot{\mathbf{B}}}{\hat{\mathbf{n}} \cdot \mathbf{V}}.$$

For an ideal (infinitely extended) sheet of FACs we obtain

$$\mu_0 j_{\parallel} = \mu_0 \mathbf{j} \cdot \hat{\mathbf{B}}_0 = \frac{|\dot{\mathbf{B}} \times \hat{\mathbf{B}}_0|^2}{(\dot{\mathbf{B}} \times \hat{\mathbf{B}}_0) \cdot \mathbf{V}},$$

since  $\dot{\mathbf{B}} \times \hat{\mathbf{B}}_0$  is aligned with  $\hat{\mathbf{n}}$ . Hence the FAC is positive/negative if the two vectors  $\dot{\mathbf{B}} \times \hat{\mathbf{B}}_0$  and  $\mathbf{V}$  form an angle smaller/larger than  $180^\circ$ . Note that in the northern hemisphere, positive FACs are downward currents, and negative FACs are upward currents. In the southern hemisphere, negative FACs are downward currents, and positive FACs are upward currents. In section 4 we show events with both polarward and equatorward crossing by Swarm spacecraft.

When multi-spacecraft information is available, one can relax part of the assumptions involved in the single-spacecraft methods to compute the FAC density. For the case of the Swarm mission, the multi-point configuration is constructed by using the low orbit SwA and SwC spacecraft. By shifting the along-track positions one can build virtual quads which make an appropriate configuration for the computation of the FAC density. Based on their computation principle, we distinguish two classes of dual-spacecraft methods. Finite differencing (FD) methods (Ritter et al., 2013; Ritter and Lühr, 2006) evaluate a discrete version of the boundary integral  $j_{\parallel} = (\mu_0 A)^{-1} \oint \mathbf{B} \cdot d\mathbf{s}$ . Linear least squares (LS) estimators (Vogt et al., 2009, 2013) are constructed by projecting the dual-satellite measurements onto a local linear magnetic field model.

While both FD and LS methods have obvious advantages over the single satellite methods, they are limited with respect to the scale resolution. The along-track separation can be varied in order to obtain squared quads configurations whereas the cross-track is limited by the orbit separation. Thus, the cross-track separation defines the lower limit of the FAC scales in the dual-spacecraft methods. The typical cross-track separation between SwA and SwC above the auroral oval is about  $\sim 70$  km.

### 2.3 Multi-scale FAC density scalogram

In order to characterize the small-scale FACs, one has to rely on single-spacecraft methods. Bunescu et al. (2015) introduced the multiscale FAC analyzer (MSMVA) to study the FAC signatures. The MSMVA technique extends the MVA analysis by providing continuous and multiscale information on the planarity and orientation of the observed FACs. The continuous character over the time domain is achieved by computing the MVA parameters (eigenvalues and eigenvectors) over a sliding window (width  $w$ ). The multiscale character is achieved by repeating the procedure for an array of window widths,  $w_k$ , within a given range (resolution  $dw$ ). The eigenvalues ( $\lambda_\eta$ ,  $\lambda_\xi$ ), eigenvectors ( $\mathbf{e}_\eta$ ,  $\mathbf{e}_\xi$ ), eigenvalues ratio,  $R = \lambda_\eta / \lambda_\xi$ , and the orientation,  $\theta \equiv \angle(\mathbf{e}_\xi, \mathbf{x})$ , are thus 2-D quantities dependent on time and scale. Bunescu et al. (2015) showed that the derivative of  $\lambda_\eta$  with respect to the length of the analysis window,  $\partial_w \lambda_\eta$ , provides the location (center) and scale (thickness) of the planar FAC



structures. The method was checked on simple synthetic FACs (infinite and finite structures) of both uniform and nonuniform FAC density and showed good performance in identifying FAC scales. The method was applied to Cluster data showing both large scale quiet arcs and locally planar and dynamic FAC structures (Bunescu et al., 2015), as well as for the analysis of conjugate Cluster/FAST observations (Bunescu et al., 2017).

- 5 The multiscale information provided by MSMVA can be used to compute other quantities, like the FAC density. MSMVA provides the scale dependent orientation that can be used to compute the FAC density into the FAC own reference system. Combined with the MSMVA results this provides a consistent tool to analyze the FAC signatures. One can compute the FAC density at each scale by discretizing equation (2)

$$j_{\parallel} = \mu_0^{-1} \Delta B_{\eta} / \Delta \xi \quad (4)$$

where  $B_{\eta}$  is computed as the projection of  $\mathbf{B}$  along the tangential direction,  $B_{\eta} = \mathbf{B} \cdot \mathbf{e}_{\eta}$ , whereas  $\Delta \xi$  is the thickness across  
 10 the structure in the normal direction. Assuming a certain velocity of the spacecraft,  $\mathbf{v}_{sc}$ ,  $\Delta \xi$  can be computed by using the projection of  $\mathbf{v}_{sc}$  on  $\mathbf{e}_{\xi}$  and the spacecraft crossing times,  $\Delta \xi = \mathbf{v}_{sc} \cdot \mathbf{e}_{\xi} \Delta t$ .

The amplitude of  $B_{\eta}$  at each scale  $w = \Delta t$  is estimated by fitting  $B_{\eta}$  using a simple linear regression analysis. Thus,  $\Delta B_{\eta} = B_{\eta}(t_b) - B_{\eta}(t_a)$ , where  $t_a$  and  $t_b$  are the limits of the analyzing window,  $w$ , at the respective position (center  $t_{cen}$  of  $[t_a, t_b]$  interval). When the analyzing scale is centered on a certain FAC structure and has the width equal to the FAC  
 15 thickness,  $\Delta B_{\eta}$  approximates well the entire perturbation across the structure. When the analysis window is centered between two balanced FACs of similar amplitude,  $j_0$ , and thickness,  $w_0$ , the two FACs cancel each other and provide no contribution to the current at that position and scale,  $\Delta B_{\eta} = 0$ . In the case of unbalanced FAC structures, the FAC density depends on their respective amplitudes and thicknesses.

The ensemble of the resulting estimates  $j_{\parallel} = j_{\parallel}(t_{cen}, w) = j_{\parallel}(t_{cen}, \Delta t)$  yields a multiscale representation of FAC density in  
 20  $(t_{cen}, w)$  space. We refer to this graphical representation as the FAC density scalogram, in analogy to the terminology used for wavelet transforms (Torrence and Compo, 1998).

## 2.4 Scale sampling schemes

We use two different FACs scanning procedures (scaling schemes) for the discretization of the FACs scale domain. The scheme implemented in (Bunescu et al., 2015) implies a linear sampling of both scale and time domain, i.e. linearly varying width for  
 25 scale space and sliding for the time space. At a given time the discretization of the scale domain is similar to the nested MVA analysis (Sonnerup and Scheible, 1998) used to study the stationarity of the MVA parameters. The minimum scale,  $w_{min}$ , is given by three points (one point on each side of the central point). Iteratively the scale increases by adding equal number of points (depending on  $dw$  resolution) to the sides of the previous scale, yielding thus an array of odd numbers,  $w_k=3,5,7..$  for the highest resolution scanning. For the Swarm high resolution magnetic field data (section 4) we look in the range between  
 30  $w_{min}=0.1$  s and  $w_{max}=5$  min which for an ionospheric mapping factor of 1.1 corresponds roughly to an ionospheric scale of about  $\sim 760$  m and  $\sim 2000$  km, respectively. This scheme has the advantage that one can scan all the FAC scales present in the data and provides a high resolution needed in the FAC scale/position identification (Bunescu et al., 2015). As discussed



in sections 3 and 4, this high resolution linear scanning introduces a large degree of correlation in the results. Indeed, for an infinite planar sheet of width  $w_0$ , this is sampled many times for all scales  $w_k \leq w_0$ . When searching for FAC scale/location this proved to be fine, since  $\partial_w \lambda_\eta$  maximized at  $w_0$ . If we are interested in the reconstruction of the FAC density time series for comparison with results usually obtained by finite differencing (equation (3)), however, a simple integration over the scales does not give the correct result. Thus, a proper weighting of the scalogram coefficients  $j_{\parallel}^{(k)}$  is required in this case, see section 2.5.

The second FAC scanning scheme uses successive intervals that do not overlap at certain scale; the length of the intervals is varied logarithmically to provide information at different scales. This scheme is similar to the one used in Haar wavelet decomposition. All scales (interval widths) spanning  $w_k = 2^k$  data points, where  $k=2, N$  ( $N$  the highest power of two that fits into the data interval) are considered. When dealing with large scales one can use zero padding of the data interval. Practically, in an ideal auroral oval configuration with balanced R1/R2 FACs, the largest scale sample the entire oval, in the second scale the interval is split into two and addresses separately R1/R2 regions. The segmentation of the data interval repeats down to the smallest scale  $w_{\min}$ . For the case of Swarm events (section 4) we take  $w_{\min} = 0.04$  (2 points) and  $w_{\max} = 21.8$  min corresponding to a total number of 16 decomposition levels. One sensitive point of this scheme is the centering of the data interval because in reality we do not have an ideal oval, e.g. one can have a tangential crossing through the oval. One can manually center the analysis interval on the border between R1 and R2 regions. The main advantage of this logarithmic scheme is that is much faster than linear scheme and provides a more intuitive understanding of the multiscale FAC density. In each computation cell of width  $\Delta \xi^{(k)}$  we have the current density  $j_{\parallel}^{(k)} = \mu_0^{-1} \Delta B_\eta^{(k)} / \Delta \xi^{(k)}$  and the integrated current  $J_{\parallel}^{(k)} = \mu_0^{-1} \Delta B_\eta^{(k)}$ . The FAC density  $j_{\parallel}^{(k)}$  reflects the slope of  $B_\eta$  whereas  $J_{\parallel}^{(k)}$  the jump of  $B_\eta$  over the respective scale,  $w_k$ . Both  $j_{\parallel}^{(k)}$  and  $J_{\parallel}^{(k)}$  offer complementary useful information. In the following we concentrate on  $j_{\parallel}^{(k)}$ , similar to linear sampling scheme.

## 2.5 FAC time series reconstruction

In both scanning procedures, linear and logarithmic, the scale array does not provide an orthogonal basis. As shown in sections 3 and 4, the FAC density is not concentrated around the FAC scale, there is a spread mainly to smaller scales. In order to compensate the dispersion of the FAC density over scales, we need a weighting function when the desire is to (partially) reconstruct a known current density by integration over the scale domain. Such a reference FAC density is available in the case of synthetic FAC structures (section 3). Based on the performance on synthetic FACs we extend to measured data (section 4), where we can also use reference FACs as provided by the two-spacecraft methods for ideal simple FACs. In the following, we use different weighting functions to compute the scale integrated current  $j_{\parallel}(\xi)$ .

$$j_{\parallel}(\xi) = \sum_k j_{\parallel}^{(k)} h^{(k)} / \sum_k h^{(k)} \quad (5)$$

where  $j_{\parallel}^{(k)}$  and  $h^{(k)}$  denote the FAC density and the weighting coefficient at the  $k$  scale. The average FAC density is obtained by considering the simplest weighting,  $h^{(k)} = 1$ . Other weighting functions can emphasis the large-scales,  $h^{(k)} = w^{(k)}$  ( $w$  the interval length), or the small-scales,  $h^{(k)} = 1/w^{(k)}$ . We denote average, large-scale, and small-scale weighting by AW, LW, and SW, respectively. The different weighting results are compared with reference FAC density profiles in section 3 and section 4.



## 2.6 Related spectral techniques

The extended MSMVA framework, and the FAC density scalogram in particular, can be compared with other spectral techniques offering spectral resolution together with time localization. The most prominent examples are the dynamical Fourier spectra produced by a windowed Fourier transformation (WFT), and wavelet techniques.

- 5 In a so-called orthogonal or discrete wavelet transform (DWT) such as the Haar transform or the Daubechies transform, the signal is represented using a family of mutually uncorrelated (hence orthogonal with respect to the canonical scalar product) basis functions. The orthogonality condition facilitates signal reconstruction but puts severe constraints on the selection of scale and time parameters that are then usually arranged in a manner similar to the logarithmic scale sampling scheme chosen for the FAC density scalogram, see subsection 2.4. A so-called continuous wavelet transform (CWT) does not aim at a compact  
 10 signal representation and hence can be based on a function family that is not constrained by orthogonality conditions. A CWT produces a (redundant) set of signal correlations with basis functions that depend on scale and time, e.g. Gaussian wave packets in the Morlet wavelet transform. In contrast to DWTs, the flexible choice of time and scale parameters in CWTs allows for a smooth representation of the time-varying scale dependence of the signal.

- The FAC density scalogram of the extended MSMVA framework introduced in this paper takes into account scale-dependent  
 15 current structure information such as sheet inclination, reflected in both perpendicular components of the magnetic field perturbation  $\Delta B$ , and thus yields a more comprehensive FAC representation than straightforward wavelet transforms could. Selected elements of wavelet transform are adopted in our constructions of FAC density scalograms, e.g., logarithmic scale sampling, and the construction of time series segments for multiscale MVA using rectangular window functions such as the basis functions in Haar wavelet transform. At the largest scale we sample the entire auroral oval, a separate sampling of R1 and R2 at the  
 20 second scale and then a progressive decrease of the analysis window appropriate for small-scale FACs, without overlapping segments. The logarithmic scheme is faster and consumes less computational resources but the analysis intervals cannot be expected to properly capture the location and extent of FAC structures.

## 3 Synthetic FAC structures

- In this section we apply the multiscale FAC density technique to synthetic structures consisting of superposed FAC activity. We  
 25 define complex FAC structures by superposing FACs of different scales (thickness), amplitude (FAC intensity), and different direction of the current flow (upward and downward). Additionally, one can consider the orientation of the FAC structure in the plane perpendicular to  $B$ . The total FAC density is given by:

$$j_{\parallel}(\xi) = \sum_k s^{(k)} j_{\parallel}^{(k)}(\xi, \xi_0^{(k)}, \sigma_{\perp}^{(k)}, \theta^{(k)}) \quad (6)$$

- where  $j_{\parallel}^{(k)}$  denotes the elementary current associated with a single FAC element;  $s^{(k)}$  is the sign of the FAC element,  $-/+$  for the upward/downward FACs. For the case of uniform FAC density structures  $j_{\parallel}^{(k)} = \text{const}$ ;  $j_{\parallel}^{(k)}$  is parametrized by the perpendicular  
 30 scale  $\sigma_{\perp}^k$ , the location of the FAC center,  $\xi_0$ , and the orientation  $\theta^{(k)}$ .



In the following, we define  $j_{\parallel}^{(k)}$  elements according to a nonuniform FAC density depending on  $\xi$  by a Gaussian function.

$$j(\xi, \xi_0, \sigma_{\perp}, \theta) = \frac{J_0}{\sigma_{\perp} \sqrt{2\pi}} e^{-(\xi \cos(\theta) - \xi_0)^2 / (2\sigma_{\perp}^2)} \quad (7)$$

Equation 7 includes a parametrization of the orientation,  $\theta$ , and reduces to the standard Gaussian function for  $\theta = 0$ . The parameter  $J_0$  indicates the integrated sheet current (integral across the arc per unit of east-west length) of a FAC element;  $\xi_0$  controls the location of the FAC element; and  $\sigma$  is the standard deviation and controls the perpendicular scale of the FAC element.

5 The standard Gaussian profile ( $\theta = 0$ ) is consistent with the FAC structures observed in the auroral region. Studies on the FAC scales (Johansson et al., 2007; Karlsson and Marklund, 1996) estimated the FAC density profile by a Gaussian function and the scale is approximated by the full-width-at-half-maximum (FWHM) estimate. FWHM is typically used also when estimating the auroral thickness from optical emissions intensity (Partamies et al., 2010). In the standard case  $\text{FWHM} = 2\sqrt{2 \ln(2)}\sigma \approx 2.35\sigma$ . In section 3.1 and 3.2 we qualitatively estimate the FAC thickness by  $w_{\perp} = 2\sigma$ .

10 The integration of the Ampere law (equation (2)) yields the magnetic field associated to the FAC density (equation (6)) given by:

$$B_{\eta} = \mu_0 \int j_{\parallel} d\xi \quad (8)$$

Considering the superposition of FACs (equation (6)), the above equation yields

$$B_{\eta} = \mu_0 \sum_k J_{\eta}^{(k)} \quad (9)$$

where  $J_{\eta}^{(k)}$  is the sheet current of the  $k$  FAC element derived as the integral of the Gaussian function and expressed in terms of error function:

$$J_{\eta}^{(k)}(\xi) = \frac{J_0^{(k)} \sec(\theta^{(k)})}{2} \operatorname{erf} \left( \frac{\xi^{(k)} \cos(\theta^{(k)}) - \xi_0^{(k)}}{\sigma \sqrt{2}} \right) \quad (10)$$

15 By using the above equations we construct two particular cases of synthetic structures. In the first case we consider a simple balanced FAC structure, consisting of an upward and a downward FAC elements of the same thickness and amplitude. The second case consists of superposed FACs, smaller scales embedded into larger FACs. We show how the multiscale FAC estimate can be used to visualize the FACs. For both cases we show the multiscale FAC density and compare the scale integrated FAC density with the input FAC density. The simple case of a pair of FACs resembles the large scale R1/R2 system, as well  
 20 as, the basic cell of a multiple arc system (Gillies et al., 2014; Wu et al., 2017). In the second case, the embedded smaller scale superposition can be associated to the analysis of the auroral oval with embedded smaller scale FACs, e.g. multiple arc systems, or pulsating aurora.

### 3.1 FAC structure of balanced current

In the following we consider the current system consisting of the upward/downward current regions. The value of the thickness,  
 25  $\sigma_{\perp}$ , for both FAC structures is 50 km. Typical values of  $\Delta B$  for the auroral region are in the range of a few 100 nT. Each



100 nT in the measured  $\Delta B$  corresponds to an integrated sheet current  $J_0 \sim 0.1$  A/m. Thus, for this synthetic case we consider  $J_0 = \pm 0.1$  A/m for the upward/downward current. The current elements are located at  $\xi_0 = 725$  km and  $\xi_0 = 875$  km. The orientation is  $\theta = 0^\circ$  for both FACs.

Figure 1 shows the results of both linear and logarithmic scale sampling for this simple FAC structure. Panel 1a1 shows the input current density,  $j_{\parallel}$ , whereas panel 1b1 the obtained magnetic field profile (equation 9). This magnetic field contains a superposed normal distributed noise signal with zero mean and sigma of 0.5 nT. The results of linear MSMVA scanning of the FAC system are shown in panels 1c1, 1d1, and 1e1 by the planarity  $R_{\lambda}$ , the derivative  $\partial_w \lambda_{\eta}$ , and the linear multiscale FAC density, respectively. The width array used in the linear MSMVA is between 1 km and  $\sim 400$  km with a step of  $\sim 0.2$  km. We note the smooth variation of all quantities specific to this sampling scheme.  $\partial_w \lambda_{\eta}$  correctly identifies the scales of the two FAC regions around  $w_{\perp} = 100$  km. The multiscale FAC density shows higher intensity at small-scale and decreasing amplitude at large scales, consistent with the overall portion of  $\Delta B$  included at each scale. The FAC density is not concentrated around the FAC scale as shown by  $\partial_w \lambda_{\eta}$  but spreads to large and small scales.

In panel 1f1 we show the different weightings (equation 5) influence on the multiscale FAC density as compared with the input current density. The black line shows the input reference FAC density, whereas blue, red, and green indicate the AW, SW and LW FAC estimates. The weighting estimates are computed over all scales. By comparing the amplitudes of the input FAC with the weighting estimates we observe that SW provides better results. AW and LW show smaller amplitudes with respect to the input FAC density. The SW shows a fluctuation level superposed on the large scale trend. The increase of the noise level in the input signal leads to an increase of the noise level in SW estimate whereas the other weightings are less affected. All weighting estimates, AW, LW, and SW are dependent on the scale domain. A larger scale range results in lower values of the AW and LW estimates in the linear approach. In order to reduce the noise level in SW for the Swarm events (section 4) we performe the weighting for scales larger than a certain treshold.

Panels 1c2-1f2 show the results of logarithmic FAC scale scanning. For this case the analysis is centered in the middle of the FAC structure, indicated by the vertical black line. The sampled scale array covers 13 logarithmic levels from  $w_{\min} = 0.2$  km to  $w_{\max} = 820$  km. The logarithmic scheme show a more discrete character due to the non-overlapping sampling intervals at each scale. The multiscale FAC density (panel 1e2) shows at the largest scale a zero current because the two structures are symmetric and compensate each other. At around 100 km we observe the separation of the two branches of the current centered at 725 km and 875 km. The distinction between the two regions is very clear down to smaller scales of a few km. Higher FAC intensity is observed around the centers of the FACs in the range of scales between  $\sim 10$  km to  $\sim 80$  km. For the logarithmic scanning the scale integrated FAC estimates are shown in panel 1f2. The three weightings are applied to scales larger than 3.2 km to avoid the noise at small-scales. SW weighting (red) provides again closer results to the input FAC density (black). AW estimate (blue) provides better results in this case as compared to the linear scanning. In this case the limited number of scales is better suited to the data interval.



### 3.2 Superposition of Gaussian FAC structures

We start again with a large scale current system similar to the previous synthetic case. Two FAC elements with  $\sigma_{\perp}=50$  km and  $J_0 = \pm 0.4$  A/m, placed at  $\xi_0=700$  km and  $\xi_0=850$  km. A number of eight small-scale FACs are superposed on this structure. We consider equal scales and amplitudes of the embedded FACs given by  $\sigma_{\perp}=20$  km, whereas their integrated sheet currents are  $J_0 = \pm 0.12$  A/m alternatively positive and negative. For simplicity we consider again  $\theta = 0^\circ$  for all FAC elements. The number of small-scale FACs and their scale were chosen in order to introduce amplitude changes of the peak current density at large-scale and also to have small regions where the two scale FACs partially cancel each other, e.g. rather zero FAC density.

Figure 2 shows the overall contribution of the two scales to a symmetric FAC density profile shown by the thick black line in panel 2a1 and the corresponding magnetic field perturbation in panel 2b1. The normal distributed noise signal has sigma of 2 nT in this case. In this example we perform the linear FAC scanning over the range between 1 km and 400 km, whereas the logarithmic scanning over the scale domain from 0.01 km up to 1310 km. The total number of levels in the logarithmic scanning is  $k=18$ . The weighted FAC estimates are computed for all scales in the linear case, whereas for the logarithmic case we use scales larger than 2.5 km. As in the previous example, we use this lowpass filtering to avoid the effect of noise at small-scales.

Panels 2c1-f1 and Figure 2c2-f2 show the MSMVA decomposition into the linear and logarithmic scheme, respectively. We notice the same characteristics of the two schemes, namely smooth and coarse results in the linear and logarithmic scanning, respectively. The combined use of  $\partial_w \lambda_{\max}$  and  $j_{\parallel}$  spectra allows the identification of the scales and the estimate of the local FAC density present at the respective scale. The linear approach shows a high precision in the identification of both FAC scale (panel 2c2) and local FAC density (panel 2e1). This scheme is associated with an over-determination of the global FAC density. The logarithmic scheme lacks resolution in the FAC scale identification and subsequently gives a poor estimate of local current. However, this scheme provides quick results that capture qualitatively similar features and, moreover, the AW estimate of the global FAC density is close to the actual value.

## 4 Auroral region crossing by Swarm

The FAC density scalogram introduced in Sect. 2 and the other components of the multi-scale FAC analyzer framework are now applied to three auroral crossings of the Swarm satellites, namely, a stable linear east-west aligned current sheet, an auroral pattern with sharp changes in inclination, and small-scale auroral structures embedded in a large-scale current.

### 4.1 Instrumentation and basic data processing

The Swarm mission (Friis-Christensen et al., 2008) consists of three spacecraft equipped with identical instruments and placed on polar orbits. The primary objective of the Swarm mission is to study the Earth magnetic field, e.g. mapping, modeling, separation of the different sources of the measured field. The satellites are equipped with both a vector field magnetometer



(VFM) and an absolute scalar magnetometer (ASM) (Hulot et al., 2015) which provide high accuracy and high resolution magnetic field measurements. ASM data are used mainly for the calibration of VFM.

In this work we mainly use the VFM measurements to study the FACs. Because we address the multiscale aspect of the FACs signatures and in order to have a good statistics also at smaller scales, we use the highest resolution data provided by VFM, namely the 50 Hz data (0.02 s sampling). The resolution of the data is directly related to the scale of the structures that can be resolved by MSMVA. For a minimum scale of 5 points in the MSMVA analysis we obtain an along-track scale mapped to ionosphere of about 760 m (spacecraft velocity of 7.6 km/s).

One major point of the Swarm constellation is its orbital configuration. Two spacecraft, SwA and SwC, are flying side by side at 460 km altitude with a cross-track separation (longitudinal separation) of  $1.4^\circ$  which amounts to about 70 km above the auroral oval. The measurements provided by these satellites are combined in the two-satellite methods to estimate the FAC density (Ritter and Lühr, 2006; Ritter et al., 2013; Vogt et al., 2013). The other spacecraft, SwB, is flying at higher altitude and periodically forms a close three-satellite configuration with the lower pair. When this is the case, it is possible to compute the FAC density by using a three-spacecraft method (Vogt et al., 2009). In the following, for each event we cross-check the integrated multiscale FAC density estimate with the dual-spacecraft estimates.

The dual-spacecraft FAC estimate provided by ESA (part of the Swarm L2 product available at <ftp://swarm-diss.eo.esa.int/>) is based on the FD approach and is provided with 1 s resolution. The dual-spacecraft LS estimate is computed with a similar 1 s resolution. The computation of FD and LS FAC estimates is done over a filtered magnetic field perturbation. The filtering is used to remove the small scales FACs with scales smaller than  $\sim 20$  s, corresponding to along-track scales smaller than  $\sim 150$  km (Lühr et al., 2016).

The second type of data used in this study is provided by the THEMIS ASI ground network. THEMIS ASI network (Donovan et al., 2006; Mende et al., 2009) was installed to complement spacecraft observations, e.g. by THEMIS mission, related to substorm and, more generally, auroral phenomena. With a number of 22 stations the network cover a large region of northern Canada, Alaska and Greenland. The THEMIS ASI locations were chosen based on an earlier statistical study (Frey et al., 2004) of the auroral substorm onsets inferred from IMAGE spacecraft. Each ASI provides frames of  $256 \times 256$  pixels at a time resolution of 3 s (exposure time 1 s). All ASI are based on fish-eye lenses that provide wide angle optical observations. Due to the fish-eye lenses the pixels on the center cover a smaller sky surface element as compared to the pixels located towards the edges. Thus, the best resolution is in the center, about 1 km. The events included in this study make use of optical data from Sanikiluaq (SNKQ), Rankin Inlet (RANK), and Fort Smith (FSMI).

One basic data analysis is the field line tracing of the spacecraft orbit. The spacecraft mapping is done by using the THEMIS TDAS software (<http://themis.ssl.berkeley.edu/>) where the field line tracing is implemented by using different versions of the Tsyganenko magnetic field model. In this paper we use Tsyganenko T04 model (Tsyganenko and Sitnov, 2005) with the solar wind parameters provided by OMNI (<http://omniweb.gsfc.nasa.gov>) and DST index from WDG at Kyoto (<http://wdc.kugi.kyoto-u.ac.jp/>). The footprints of Swarm are superposed on the optical data provided by the THEMIS ground stations.



The measured magnetic field is transformed to the MFA reference system. The magnetic field perturbation,  $\Delta B$ , is obtained by subtracting a model magnetic field from the measured data. The internal magnetic field parametrization is taken from CHAOS-6 (Olsen et al., 2014; Finlay et al., 2016) whereas the lithospheric (e.g. crust and upper-most mantle) and external magnetospheric (e.g. ring current) contributions are taken from the Pomme 10 (Maus et al., 2006, 2010) model. The results  
5 obtained for various events in different geomagnetic conditions showed good consistency when using this setup. Ideally, after the subtraction of the magnetic field model we should remain with the perturbation caused by the large scale R1/R2 currents, the embedded mesoscale and small-scale FACs, as well as the influence of the ionospheric current systems. Another option is to separate the embedded small-scales FACs from the large-scale FACs (R1/R2) by filtering the data. Bunescu et al. (2015) computed a model magnetic field proxy from the measured field using an average over a sliding window (with tapering at the  
10 ends). This procedure excludes roughly the scales smaller than a certain percent of the sliding window width (depending on the tapering extent). The disadvantage of this approach is that it can introduce additional low amplitude fluctuations. Thus, in the following we analyze  $\Delta B$  obtained by subtracting the model magnetic.

#### 4.2 Stable east-west aligned aurora of constant FAC density

On 17 February 2015 the Swarm spacecraft crossed the auroral oval toward north over the FoV of the SNKQ station. The  
15 event is observed around 03:25 UT at  $\sim 1$  h after an intermediate substorm intensification/onset following  $\sim 6$  h of quasi-steady magnetospheric convection. The AE index is  $\sim 200$  nT, whereas  $DST \sim -26$  nT.

Figure 3 shows the ionospheric footprints of the spacecraft (mapping at 110 km altitude) superposed on the SNKQ optical observations. The optical data show rather stable and east-west elongated arc structures. We distinguish two large-scale upward FACs located northward and, respectively, further southward of the station. Between these two upward FACs we observe a  
20 mesoscale upward FAC with an east-west extent covering the westward FoV of SNKQ. The stability of the arcs is confirmed by the optical frames showing highly planar auroral arcs. Swarm is crossing along the westward edge of the ASI over all three visible arcs.

Figure 4a shows the keogram from SNKQ obtained by stacking in time the central column (meridian) of pixels from the optical frames. The combined analysis of optical frames and of SNKQ keogram confirm the stability of the aurora over the  
25 entire interval. The intermediate arc appears in the center of ASI around 03:25 UT. The measured  $\Delta B_{\perp}$  by SwA/SwC are shown in Figure 4b-c.  $\Delta B_{\perp}$  from both spacecraft shows similar structures, with a small difference in amplitude, consistent with optical data.  $\Delta B_{\perp}$  from SwA shows a shift (within 10 s) with respect to SwC crossing earlier. SwB (not included) is not properly located, its footprint is outside the ASI's FoV. The vertical dashed lines indicate distinct regions of the FAC system. The black, blue, and green indicate the beginning of upward FACs labeled U1, U2, and U3 whereas magenta and cyan indicate  
30 the downward regions in-between, labeled D1 and D2. One observes some small imbalance between the upward and downward current, presumably caused by a cross-polar cap current system, or by the imprecision of the magnetic field model in the polar region.

Figure 4d-e shows different FAC density estimates. The green and red line (Figure 4d) shows the L2 single-spacecraft FAC density obtained using the un-filtered magnetic field data from SwA and SwC, respectively. The L2 single-spacecraft FAC



estimate (Ritter et al., 2013) is computed with the assumption that the main magnetic perturbation is in the east-west  $B_y$  component. Panel 4e shows the dual-spacecraft FAC density that combines the information provided by SwA and SwC. The magenta/blue lines indicate the FD/LS estimate based on (Ritter et al., 2013)/(Vogt et al., 2013) method. The two estimates correspond to the same resolution of the filtered data. One can notice that both FD/LS estimates provide roughly similar results.

5 The observed time shift is artificial, caused by the way one assigns the time baseline to the FAC profile, i.e. using swA (L2) or swC (LS) time tags. The two-spacecraft methods show an average of the FAC density over the quad area and do not capture small-scale FACs. Both single and dual-spacecraft FAC estimates are used as a qualitative reference for our multiscale FAC density technique.

The right part of Figure 4f shows the hodogram representation,  $B_y$  as a function of  $B_x$ , for SwA. The hodogram is represented with the time interval running from blue to red. The FAC segments have the same color used in Figure 4a-e to mark the beginning of the respective time interval. We observe different regions of the hodogram that consist of linear segments which indicate FAC structures of constant orientation (linear polarization of  $\Delta B$ ). The U1, U2, and U3 FACs are indicated by the black, blue, and green lines, respectively. The MSMVA is used to find and characterize such segments of linear polarization of  $\Delta B$ .

10

The left part of Figure 5 shows the results of the linear MSMVA for SwA. The planarity, shown by  $R_\lambda$  spectrogram (panel b1), indicates regions of high planarity for several large/small-scale FACs, e.g. U1-3 and D1-2. The spectrogram of  $\partial_w \lambda_\eta$  (panel c1) shows the location and thickness of FAC structures whereas their orientation (panel d1) is given by the angle between the FAC's normal and the north MFA direction. Some typical threshold value of  $R_\lambda$  associated to planar structures is about 10-30 (for 3D MVA). Because we use the 2D MVA ( $B_\perp$  perturbation),  $R_\lambda$  shows larger values, consistent with a reduced variance.

15

20 We note that the investigation of the relationship between the longitudinal extension of FACs and the  $R_\lambda$  ratio can actually be done by using correlation analysis of the two longitudinally separated Swarm spacecraft. One can expect that  $R_\lambda$  can provide a more quantitative indication about the FAC length. This topic is considered for a future study.

Panel 5e1 shows the newly introduced linear multiscale FAC density (section 2). We can easily see the different regions of upward and downward current at different scales, e.g. large-scale R1/R2 FACs at scales larger than 100 s and smaller scale FACs (U1-3, D1-2) at lower values. Panels 5f1 and 5g1 show the scale integrated FAC density obtained by using the LW (black) and SW (red) weightings, respectively. AW typically provides lower amplitudes and was not included. In panel 5g1 SW is compared to the L2 single-spacecraft FAC (black) and the dual-spacecraft LS FAC estimate (blue). The LS dual-spacecraft profile is slightly shifted in time because it is linked to swC time-tags. In order to reduce the fluctuation level caused by the small-scale FACs, the SW estimate is computed over scales larger than 1 s ( $\sim 7$  km ionospheric scale). SW FAC estimate shows consistent results with the single- and dual-spacecraft FAC estimates. Note that the single-spacecraft estimate is computed for the 1 s resolution of  $\Delta B$  whereas the computation by MSMVA goes down to 0.1 s (5 points). The LW FAC separates well the R1/R2 FAC regions and identifies the oval center. One can use the minimum/maximum of this estimate as a proxy for the identification of the R1/R2 centers. The negative/positive large-scale trend is associated to upward/downward FACs, consistent with the statistical FAC model (Iijima and Potemra, 1976b) around 03.30 MLT. An alternative identification of the large-scale FACs is done by

25

30



(Wu et al., 2017) directly with single-spacecraft FAC density by computing the ratio of the upward and downward current to the total current.

These representations provide a new visualization of the FAC currents dependent on scale. The linear scanning of FACs uses a large number of scales sampled at high resolution. As already mentioned, one limitation in the integrated FAC estimate for this approach is that it does not rely on an orthogonal basis and thus the integration over scales depends on the scanning parameters. In order to partially improve the analysis towards an orthogonal basis we compute the same parameters for the logarithmic scanning procedure (section 2). Panels 5b2-g2 show MSMVA quantities for the logarithmic scanning. In this case the scale range extends to higher values ( $\sim 1000$  s=16.6 min) and from about 300 km up one can see a close to zero net current. AW estimate provides roughly similar results with SW from the linear approach. Considering the uniform FAC segment U1 we notice that both scanning procedures, SW and AW, give slightly lower amplitudes as compared to the standard L2 FAC estimate. On D1 we observe better agreement between SW/AW and the dual-spacecraft estimate, whereas on U2 we see a similarity between SW/AW and the single-spacecraft estimate. In the same panel one can notice the presence of small-scale FACs which are not visible in the LS estimate. The resolution is not suitable to obtain precise information on the scale dependence of these quantities. The results are in good qualitative agreement with the linear scanning.

Figure 6 shows a more quantitative comparison of the MSMVA quantities, including FAC density given by the two scanning schemes. We show the scale dependence of  $R_\lambda$ ,  $\partial_w \lambda_\eta$ ,  $\theta$ , and  $j_\parallel$  at the center of the FACs as identified by  $\partial_w \lambda_\eta$  and indicated by the solid lines in Figure 5. The selected times are  $t_{U1}=03:24:43$  and  $t_{D1}=03:25:00$ , associated to U1 and D1, respectively. One can see that all quantities have local maxima around the same scale indicated by the vertical dash lines at 25 s and 10 s for U1 and D1, respectively. These scales correspond to about 170 km and 70 km in the ionosphere.  $R_\lambda$  shows a high planarity at these two scales. We note a shift of the local maxima of  $R_\lambda$  as compared to the other quantities, possibly related to the contribution from  $\lambda_\xi$ . The FAC density at U1 and D1 structures is around  $-2.5 \mu A/m^2$  and  $1.5 \mu A/m^2$ , respectively, for the linear sampling. In the case of logarithmic sampling,  $j_\parallel$  (dashed lines in panel 6d) shows roughly similar results where the respective scales are properly sampled. We have agreement for U1 ( $\sim -2.5 \mu A/m^2$ ) and a lower FAC density ( $0.5 \mu A/m^2$ ) for D1. The low estimate of the current for D1 in the logarithmic scanning is caused by imperfect centering at that scale with respect to the linear scanning. The profile of  $j_\parallel$  for D1 corresponds to the same scale, but it is evaluated in a different point with respect to  $t_{D1}$ . For the logarithmic scheme, precise comparison with the linear scheme can be obtained at the centers of the sampled intervals (panel 5e2).

Through the continuous and multiscale MSMVA analysis we identify the discrete FAC elements associated to the measured magnetic field perturbation. The sections in the MSMVA spectra quantify how much current one has at the respective FAC structure. The results show the difficulty of dealing at the same time with a meaningful FAC density estimate at a given scale and the need for orthogonality in the MSMVA basis functions. While FAC density is correctly inferred locally, the lack of orthogonality results in deviations from the actual value for the global FAC density. The sections shown in Figure 6 were selected around the local maximum of  $\partial_w \lambda_\eta$ . The sharp maximum of  $\partial_w \lambda_\eta$  for U1 and D1 agrees with structures of constant current densities (Bunescu et al., 2015), also expected from the  $\Delta B$  profile. The gray shaded area in Figure 6 shows the range of scales for which  $R_\lambda$  is below an arbitrary reference level of 100. This indicates the possibility to clean MSMVA quantities



based on the planarity level. Such an option is needed for a multi-event or statistical study on the scale dependence of FACs characteristics. Overall, the sections into the MSMVA spectra indicate consistent results, since all quantities show roughly the same scale. One can also note that the linear scheme is better suited for scale analysis.

A comparison of the regular single-satellite FAC density with the MVA corrected FAC density product, albeit without scale dependence, is included also in Gillies et al. (2015) for 9 events of pulsating aurora. Gillies et al. (2015) found consistent results between the two estimates at the edges of the patches associated to  $R_\lambda = \lambda_{\text{int}}/\lambda_{\text{min}} > 10$  for which the infinite FAC sheet approximation was considered valid, whereas, within the patch the criteria  $R_\lambda > 10$  was fulfilled only for 5 out of 9 events.

The multiscale FAC density benefit from the orientation computed at each scale. For the case of east-west aligned FACs, this may have less influence, even though one cannot exclude that some FAC elements, in a certain range of scales, are not east-west aligned. The more so, one can expect differences for events of inclined FACs. Typically, the quiet aurora during the growth phase has the normal direction aligned with the north direction. By using the multiscale approach one can check if this is true also for the embedded small-scale FACs. During the onset, expansion, or early recovery phase the aurora is typically dominated by 2D forms, possibly including locally planar small-scale FACs. By using the multiscale estimates one can quantify better the FACs with respect to their orientation as a function of scale. This might help to quantify whether the embedded FACs are forced to have the same orientation as the large-scale FACs and, further on, possible relationships between the respective mechanisms. The FAC density spectrogram combined with the other information of MSMVA provides a more intuitive and visual representation that can help to search the data for particular information.

### 4.3 Inclined and periodic auroral structures

This event was observed by Swarm and RANK station of the THEMIS ASI network on 15 January 2015 around 07:39 UT. The event is observed after a long quiet period, during the growth phase of a substorm with maximum  $\sim 1$  h later and, possibly, during/after pseudo-breakup activity. The AE index is  $\sim 70$  nT and DST between  $-5$  and  $-8$  nT. The optical frames under the spacecraft track (07:39:27-07:39:54) are shown in Figure 7. The optical frames from the southward pass of Swarm over RANK were not included since the structures are not clearly visible.  $\Delta B$  shown below indicates locally planar FACs also in this region. In the center of RANK SwA/SwC are crossing different structures. The apparently larger distance between the mapped points over the central region of the frames is related to the fish eye lens which distorts the aurora. The two planar FACs are about parallel as shown also by the magnetic field data below. The optical data show periodic signatures of planar structures inclined with respect to east-west direction by about  $20^\circ$ . The RANK keogram (panel 8a) shows a patchy character related to the structuring of aurora. While not detailed here, a more consistent display of the time evolution of aurora can be obtained through the satellite-aligned keograms SAK (Gillies et al., 2015) obtained by stacking in time the line of pixels along the spacecraft trajectory. This is particularly useful for small-scale structures, e.g. pulsating auroral patches (Gillies et al., 2015).

Consistent with the inclination of the FAC structures, we have a stronger northward  $B_x$  component of  $B_\perp$  up to about 100 nT. One can expect that the calculation of the typical single-spacecraft FAC density that neglects  $B_x$  component would lead to an underestimation of  $j_\parallel$ . Figures 8b and 8c showing Swarm measurements of  $\Delta B$  indicate similar FAC structures observed



by SwA and SwC. Without optical data one could think that the two spacecraft are crossing the same structures, because of the similarity of  $B$  signatures, possibly with same dynamics considering that  $B_x$  component is varying. The L2 single-satellite FAC density (data at 1 s resolution), shown in Figure 8d, indicates an oscillatory signature, associated to crossing a sequence of upward and downward FACs. The oscillations are also shown by the two-spacecraft products, FD and LS estimates (Figure 8e). One can expect that the two-spacecraft estimate is rather not suitable to describe this event because the assumption of uniformity over the quad surface is likely not well satisfied. The two-satellite methods can average over different structures. In this respect, the scanning of FACs by using MSMVA can help to visualize and characterize the consistency between SwA and SwC observations of geometry ( $R_\lambda$ ) and orientation ( $\theta$ ). For completeness, Figure 8f shows the hodogram for this event. The intervals and the color code assignment is the same as for the previous event. Moving towards higher latitudes, SwA is crossing successively several upward and downward FAC segments colored by black, magenta, blue, cyan, green, yellow, red, and black in the hodogram. We label the delimited upward FACs by U1-U4 and the downward regions by D1-D4. The magenta interval shows also a substructure of three FACs. The difference with respect to the previous case is that for this event we have a more complex current system with embedded mesoscale FACs superposed mainly on the large-scale upward FAC, consistent with the optical data.

Figure 9 shows the results of the multiscale analysis for SwA. The left/right plots show the comparison of linear/logarithmic scanning schemes.  $R_\lambda$  shows high values for the mesoscale FAC structures in the southern part of RANK location, not well visible optically. Higher values are also associated with the crossing of the FAC system in the center of FoV, where  $\partial_w \lambda_\eta$  shows high intensity for U4 and D4 regions. The scale associated to U4 and D4 region is around 10 s (70 km). The orientation at these scales is  $\sim 0^\circ$  and  $\sim 20^\circ$ , respectively, qualitatively consistent with the optical data. The  $j_{\parallel}$  spectra (panels e1 and e2) show well the embedded regions of upward and downward directed current. One can zoom into this display to get information at smaller scales, e.g. the region adjacent to the equatorward part of the track.

As in the previous event, we compare the results of the integrated FAC density with the single- and dual-spacecraft estimates. Panels 9f1-g1 and 9f2-g2 show results for the linear and logarithmic scannings, respectively. When comparing the results of the single- and dual-spacecraft estimates, we observe a general trend of anti-phase FAC density given by the LS dual-spacecraft estimate with respect to single-spacecraft and the weighting estimates. As before, the LW estimate helps to identify the oval center and the centers of the two branches of large-scale R1 and R2 current. The logarithmic scheme provides lower resolution and  $\partial_w \lambda_\eta$  does not identify the structures whereas  $j_{\parallel}$  shows well resolved regions of the FAC content. The logarithmic FAC constitute a subset of the linear FAC.

Similar to the previous event in Figure 10 we show sections across MSMVA spectra to infer quantitative estimates of the scales and current densities for a few selected FAC elements. The times of the sections are 07:38:41 (blue), 07:39:09 (green), and 07:39:33 (red). These times, indicated by the solid lines in Figure 9, are all located in upward current regions, U2, U3, U4 intervals. The maxima of  $\partial_w \lambda_\eta$  at larger scales correspond to remote FAC elements, e.g. U4 and D4 (see Figure 9). We note again the slight shift between  $R_\lambda$  local maxima and the maxima of the other quantities. We note a similar scale of  $\sim 13$  s (90 km ionospheric scale) for all three FACs. The scale dependence at these sections shows again clearly that a masking procedure based on  $R_\lambda$  is effective in removing the features associated to remote FACs crossed earlier or later. The orientation (panel 10c)



shows an inclination of about  $-20^\circ$  for U2 (blue),  $\sim 0^\circ$  for U3 (green) and  $-30^\circ$  for U4 (red) consistent with the optical data. The values of the FAC density at these FAC segments are about  $0.6\mu A/m^2$ , for both U2 and U3 and increase for the U4 (red) FAC segment to  $-1.6\mu A/m^2$ .

This event indicates that care is needed when designing an automatic procedure for the analysis of FACs on a statistical basis.

- 5 The two-spacecraft methods can average over different structures, moreover some assumptions of the methods are possibly not fulfilled. In this respect, the scanning of FAC signatures by using MSMVA might help to check the consistency between SwA/SwC observations of planarity and orientation.

#### 4.4 Small scale auroral observations embedded into a large scale current

The relation between multiple arc systems and their FAC signatures was addressed recently by (Wu et al., 2017) based on  
10 Swarm/THEMIS ASI observations. Wu et al. (2017) selected events with clearly identifiable stable arcs and separated the observations in two categories, unipolar (multiple arcs embedded into a single large upward FAC) and multipolar events (a collection of multiple arcs and related pairs of upward and downward FACs). Arcs associated with multipolar FAC events were found to be broader and more separated than those associated with unipolar FAC events. In this section we perform MSMVA analysis for an event included in Wu et al. (2017).

- 15 The event occurred on 27 September 2014 around 06:00 UT, in the evening sector ( $\sim 22$  MLT) and was observed simultaneously by Swarm and FSMI ASI in Canada. The event is observed during a very active period, with multiple substorms and an average AE of  $\sim 500$  nT over the hours around the event. The AE index is  $\sim 550$  nT and  $DST = -23$  nT.

The optical frames and the superposed spacecraft tracks, shown in Figure 11, indicate the crossing towards equator of a thick auroral structure ( $\sim 05:59:48-06:00 = 12$  s) followed by some small-scale less intense arcs and an intense structure  
20 around 06:00:09-06:00:12. Since the crossing is near the edge of the ASI FoV in the following we do not attempt to make a one to one matching between the optical observations and  $\Delta B$  or FAC signatures. The MLT location of the event and the optical data indicate the crossing near the Harang discontinuity region. Following Swarm track (north to south) the statistical model of FACs (Iijima and Potemra, 1976b) indicates the crossing of the large-scale downward, upward, and downward FACs.  $\Delta B$  for both SwA and SwC (panels 12b-c) show the three large scale FACs with embedded smaller scale structures. The  
25 hodogram (panel 12f) shows the typical characteristics observed for the previous events. The prevalence of  $\Delta B_y$  indicates a close alignment of the arcs with the east-west direction. Embedded small-scale FACs segments are seen in the green interval. The red interval shows as well small-scale FACS and a rotation in the hodogram, specific to wave activity. The FAC density estimates are shown in panels 12d and 12e. We note the high fluctuation level in the single-spacecraft estimates caused by small-scale FACs (see also panels 13g1 and 13g2 below). The two spacecraft methods show similar large-scale FACs and do  
30 not capture small-scale currents which are dynamic since the related signatures on the two spacecraft, separated by  $\sim 10$  s in latitude, are different. The small-scale features are captured by the single-satellite FAC estimates but it is difficult to quantify their characteristics based only on this information. Comparison of  $\Delta B$  from SwA and SwC shows more clearly small-scale perturbations on SwC in the green interval. Thus, in the following we perform MSMVA analysis on SwC.



Figure 13 shows the results of the linear and logarithmic FAC scanning. The intensity of the spectra for the linear scheme is also shown in logarithmic scale to emphasize the small-scale FACs. The highly planar FACs at small-scales is confirmed by  $R_\lambda$  spectrogram (panel 13b1), consistent with the hodogram. The general description from the previous events applies also here. In the following, we concentrate on the green interval where we select and analyze in more detail a few FACs. Figure 14 shows the sections in the MSMVA spectra. We observe again that remote FACs have a smaller impact on  $R_\lambda$  as compared to  $\partial_w \lambda_\eta$ . The dependence of  $\partial_w \lambda_\eta$  on scale indicates scales between 2 s (13.8 km) and 4 s (27.6 km) for the selected FACs. The orientation shows values from  $-40^\circ$  to  $10^\circ$ , whereas the FAC density has values between  $-8 \mu A/m^2$  and  $6 \mu A/m^2$ .

When going to smaller scales, non-stationary effects become more important and can be characterized by using the nested MVA analysis. This procedure is implicitly included in the MSMVA technique since at each point we perform a nested MVA in the linear scanning. The standard nested MVA (Sonnerup and Scheible, 1998) is applied in 3D and investigates the scale dependence of orientation and projections of  $\mathbf{B}$  on the eigen vectors. In this study, we extended MSMVA analysis by the density scalogram and showed quantitative estimates of the local current density for FACs observed by Swarm.

## 5 Discussion and summary

A good fraction of the FAC signatures above the auroral oval consist of rapidly varying FAC features, associated with time dependent discrete aurora, superposed on slowly varying FAC structures (R1 and R2 currents). Using a fixed window analysis approach to study the FACs which occur at different scales has limitations. Instead, one can use varying window sizes to capture both the fast and slow varying FACs. The long/short analysis windows are appropriate for large/small-scale FACs.

The MSMVA technique was previously applied to auroral oval crossings by Cluster and FAST spacecraft. The main goal of (Bunescu et al., 2015) was to introduce the technique for the scale identification capability by  $\partial_w \lambda_\eta$ . Bunescu et al. (2015) showed large-scale planar and stable arcs as well as more dynamic aurora locally planar, but did not address in detail the superposition of scales. The magnetic field was filtered such that the large scale R1 and R2 FACs were practically removed. Thus, the method was effectively showing the sequence of crossing of mesoscale FACs whereas the small scale FACs were not analyzed in detail in terms of localization and orientation.

In order to sample all scales, the analysis was previously applied using a linear scale sampling, covered typically with high resolution. While some small scale structures are seen, as they should, in their scale range, they also contribute to the variance at large scales. One large scale is identified as planar at any scale smaller than its thickness. By using this method one can self-consistently derive various information on the planarity, scale, and also on the current density, which is particularly useful when optical data are not available in event studies.

In this study we compared the integrated multiscale FAC density estimates with well established methods used routinely for the computation of the FAC density. The goal was to show that the multiscale FAC density provides results consistent with other methods, in particular those of (Ritter et al., 2013) and (Vogt et al., 2013). Both two-spacecraft FAC density estimations provide similar results and rely to the same degree on time-stationarity, since virtual (time-shifted) measurements are combined. When



time-stationarity is less of a problem, the LS method is in principle less dependent on small-scale fluctuations since it finds a solution by minimising a cost function (deviation from a linear model).

In the case of synthetic FACs, the weighting estimates are compared with the input current density. In the linear scanning scheme SW provides better results whereas for the logarithmic scheme AW shows pretty consistent results. For the Swarm data (section 4) we compare the three weightings with the reference single and dual-spacecraft FAC and show similar results, namely that for the linear and logarithmic scheme the SW and AW estimate, respectively, provides a consistent FAC density. Because the weighting introduces a scale dependence, the integrated multiscale FAC density estimates are dependent on the scale range. In the case of the logarithmic scanning, AW provides consistent results due to the reduced number of scales and reduced correlation associated to the fixed sampling scheme. The different weightings are used for a qualitative comparison of the consistency of our results.

The analysis presented in this work offers a new visualization tool for the FAC density that helps to explore current structures embedded into larger scale FACs. The main goal of the paper is to enable the visualization of the multiscale FAC density. Based on this framework we can easily visualize the discrete constituents of a measured FAC signature.  $R_\lambda$  dependence on scale in the center of FAC structures allow to separate the instantaneously crossed FACs from remote FACs. Thus we can separate the near field FACs from the far field FACs. The accuracy of the identification depends on the relative distance between the FACs and their planarity. The complex FAC signatures can be thus deconvoluted into a discrete sequence of FAC elements.

Because MSMVA is based on the statistical MVA analysis, it can be affected by two types of error, namely the statistical and the discretization errors. At small analysis windows, well suitable for the fine scale FACs, the MVA is affected by the increase of the statistical error (noise level). Higher analysis windows, suitable for the mesoscale and large scale FACs, are associated to a lower statistical error in the MSMVA, because the analysis window include a large number of measurements. However, for large analysis windows there is an increase of the discretization error. The discretization error is caused by the use of analysis windows larger than the FAC signature, in which case the FAC is not well sampled. The error analysis of MSMVA is not the subject of this paper and it will be addressed in a future publication.

The dual-spacecraft FD and LS, estimates can be unreliable in the case of dynamic and/or periodic auroral structures, as shown in section 4.3. Gillies et al. (2015) also pointed out that the two-spacecraft products can be compromised in regions of diffuse aurora, typically observed near the equatorward of the auroral oval, around the midnight sector following substorms. When applied to pulsating aurora Gillies et al. (2015), the dual-spacecraft approach, does not precisely identify the boundaries of the auroral patches associated to FAC reversals, whereas the single-spacecraft precisely identifies these boundaries. One region of interest to apply MSMVA is adjacent to the polar-cap. This region is known for the high variability of the FAC geometries, typically filamentary. For such dynamic and non-planar events two-spacecraft methods are used to derive the FAC density (Lühr et al., 2016). By using MSMVA one could obtain visual information on the consistency of these results as well as on (non)planarity.



## 6 Conclusions and outlook

The technique presented in this paper provides a multiscale version of the single-spacecraft FAC density estimate. The main goal of this technique is to assist the studies of aurora by an improved visualization of the FAC structures.

The application of the technique to measured data showed that the multiscale FAC density can provide results that are consistent with the typically used methods. We applied the MSMVA technique for the computation of multiscale FAC density using two scale scanning procedures, the linear and the logarithmic. We also showed the scale integration of the multiscale FAC density by using the average and the biased weightings towards large and small scales. We showed that the small scale weighting of the multiscale FAC density provides better consistency for the linear scanning procedure, whereas the average estimate provides better consistency for the logarithmic scanning procedure.

Future work will address an error analysis of the multiscale information. We plan to use the bootstrap method to evaluate the impact of the error level of the input magnetic field perturbation on the output multiscale information. The multiscale approach offers a good setup to study the distribution of the error caused by the statistical error (noise level), predominant at small scales, and the discretization error (imperfect sampling of the FACs), predominant at large scales, where the analysis window becomes larger than the FAC signature. We expect thus to properly separate between different error sources of the multiscale information, e.g. multiscale FAC density, FAC localization, thickness, and orientation.

So far the method does not properly take into account the geometry of the FAC structures. At this point one can select thresholds in the planarity and, accordingly, apply a mask to other quantities. Masked results were not included since they affect the overall structure of the displayed quantities. However, the masks are suitable to select a certain type of FACs, e.g. planar or non-planar. Further improvement might address a thorough study on finite structures to properly quantify the influence of the scale and how the planarity can better weight the results. In this respect we plan to extend the method to a dual-spacecraft multiscale analysis by using Swarm observations. With two satellites one can correlate the quantities, e.g. planarity, along longitude.

Swarm provides an appropriate platform to quantify and check the planarity as provided by eigenvalue ratios based on the similarity of the results obtained from the two longitudinally separated measurement points. This analysis is particularly useful for the fine structure of the aurora which cannot be addressed by other dual-spacecraft methods due to the spacecraft configuration limitations.

At present, the scale dependence of FACs properties can be investigated using Swarm, FAST, and Cluster high-resolution measurements. The technique can be easily adapted to other more recently launched missions, like MMS, particularly for conjugate measurements, e.g. MMS/Swarm.

*Acknowledgements.* We acknowledge the supported from the Deutsche Forschungsgemeinschaft (DFG) through grant VO 855/4-1 MuSICAL in the context of the DFG Priority Programme SPP 1788 DynamicEarth. Additional support by SIFACIT project with ESA, contract 4000118383/16/I-EF. We acknowledge the use of the conjunction finder interface available at <https://swarm-aurora.com/conjunctionFinder/>. We acknowledge the use of the Swarm magnetic field data as well as the L2 products provided by ESA at <ftp://swarm-diss.eo.esa.int/>. We



acknowledge NASA contract NAS5-02099 and V. Angelopoulos for the use of data from the THEMIS Mission, specifically, S. Mende and E. Donovan for the use of the ASI data (<http://themis.ssl.berkeley.edu/data/themis/thg/>), the CSA for logistical support in fielding and data retrieval from the GBO stations, and NSF for support of GIMNAST through grant AGS-1004736. We acknowledge the use of THEMIS Data Analysis Software available at <http://themis.ssl.berkeley.edu/>. The Tsyganenko magnetic field model involves the use of the DST and OMNI data. The DST data are provided by the World Data Center for Geomagnetism, Kyoto (<http://wdc.kugi.kyoto-u.ac.jp/>). The OMNI data were obtained from the GSFC/SPDF OMNIWeb interface at <http://omniweb.gsfc.nasa.gov>.



## References

- Bunescu, C., Marghitu, O., Constantinescu, D., Narita, Y., Vogt, J., and Blăgău, A.: Multiscale field-aligned current analyzer, *Journal of Geophysical Research: Space Physics*, 120, 9563–9577, <https://doi.org/10.1002/2015JA021670>, <http://dx.doi.org/10.1002/2015JA021670>, 2015.
- 5 Bunescu, C., Marghitu, O., Vogt, J., Constantinescu, D., and Partamies, N.: Quasiperiodic field-aligned current dynamics associated with auroral undulations during a substorm recovery, *Journal of Geophysical Research: Space Physics*, 122, 3087–3109, <https://doi.org/10.1002/2016JA023251>, <http://dx.doi.org/10.1002/2016JA023251>, 2017.
- Chaston, C. C., Peticolas, L. M., Bonnell, J. W., Carlson, C. W., Ergun, R. E., McFadden, J. P., and Strangeway, R. J.: Width and brightness of auroral arcs driven by inertial Alfvén waves, *Journal of Geophysical Research: Space Physics*, 108, <https://doi.org/10.1029/2001JA007537>, <http://dx.doi.org/10.1029/2001JA007537>, 2003.
- 10 Donovan, E., Mende, S., Jackel, B., Frey, H., Syrjäso, M., Voronkov, I., Trondsen, T., Peticolas, L., Angelopoulos, V., Harris, S., Greffen, M., and Connors, M.: The {THEMIS} all-sky imaging array—system design and initial results from the prototype imager, *Journal of Atmospheric and Solar-Terrestrial Physics*, 68, 1472 – 1487, <https://doi.org/http://dx.doi.org/10.1016/j.jastp.2005.03.027>, <http://www.sciencedirect.com/science/article/pii/S1364682606001118>, *passive Optics AeronomyPassive Optics Workshop*, 2006.
- 15 Finlay, C. C., Olsen, N., Kotsiaros, S., Gillet, N., and Tøffner-Clausen, L.: Recent geomagnetic secular variation from Swarm and ground observatories as estimated in the CHAOS-6 geomagnetic field model, *Earth, Planets and Space*, 68, 112, <https://doi.org/10.1186/s40623-016-0486-1>, <http://dx.doi.org/10.1186/s40623-016-0486-1>, 2016.
- Forsyth, C., Rae, I. J., Mann, I. R., and Pakhotin, I. P.: Identifying intervals of temporally invariant field-aligned currents from Swarm: Assessing the validity of single-spacecraft methods, *Journal of Geophysical Research: Space Physics*, 122, 3411–3419, <https://doi.org/10.1002/2016JA023708>, <http://dx.doi.org/10.1002/2016JA023708>, 2017.
- 20 Frey, H. U., Mende, S. B., Angelopoulos, V., and Donovan, E. F.: Substorm onset observations by IMAGE-FUV, *Journal of Geophysical Research: Space Physics*, 109, <https://doi.org/10.1029/2004JA010607>, <http://dx.doi.org/10.1029/2004JA010607>, 2004.
- Friis-Christensen, E., Lühr, H., Knudsen, D., and Haugmans, R.: Swarm – An Earth Observation Mission investigating Geospace, *Advances in Space Research*, 41, 210 – 216, <https://doi.org/https://doi.org/10.1016/j.asr.2006.10.008>, <http://www.sciencedirect.com/science/article/pii/S0273117706005497>, 2008.
- 25 Gillies, D. M., Knudsen, D. J., Donovan, E. F., Spanswick, E. L., Hansen, C., Keating, D., and Erion, S.: A survey of quiet auroral arc orientation and the effects of the interplanetary magnetic field, *Journal of Geophysical Research: Space Physics*, 119, 2550–2562, <https://doi.org/10.1002/2013JA019469>, <http://dx.doi.org/10.1002/2013JA019469>, 2014.
- Gillies, D. M., Knudsen, D., Spanswick, E., Donovan, E., Burchill, J., and Patrick, M.: Swarm observations of field-aligned currents associated with pulsating auroral patches, *Journal of Geophysical Research: Space Physics*, 120, 9484–9499, <https://doi.org/10.1002/2015JA021416>, <https://agupubs.onlinelibrary.wiley.com/doi/abs/10.1002/2015JA021416>, 2015.
- 30 Gjerloev, J. W., Ohtani, S., Iijima, T., Anderson, B., Slavin, J., and Le, G.: Characteristics of the terrestrial field-aligned current system, *Annales Geophysicae*, 29, 1713–1729, <https://doi.org/10.5194/angeo-29-1713-2011>, <http://www.ann-geophys.net/29/1713/2011/>, 2011.
- He, M., Vogt, J., Lühr, H., Sorbalo, E., Blagau, A., Le, G., and Lu, G.: A high-resolution model of field-aligned currents through empirical orthogonal functions analysis (MFACE), *Geophysical Research Letters*, 39, <https://doi.org/10.1029/2012GL053168>, <http://dx.doi.org/10.1029/2012GL053168>, 2012.
- 35



- Huang, T., Lühr, H., and Wang, H.: Global characteristics of auroral Hall currents derived from the Swarm constellation: dependences on season and IMF orientation, *Annales Geophysicae*, 35, 1249–1268, <https://doi.org/10.5194/angeo-35-1249-2017>, <https://www.ann-geophys.net/35/1249/2017/>, 2017.
- Hulot, G., Vigneron, P., Léger, J.-M., Fratter, I., Olsen, N., Jager, T., Bertrand, F., Brocco, L., Sirol, O., Lalanne, X., Boness, A., and Cattin, V.: Swarm's absolute magnetometer experimental vector mode, an innovative capability for space magnetometry, *Geophysical Research Letters*, 42, 1352–1359, <https://doi.org/10.1002/2014GL062700>, <http://dx.doi.org/10.1002/2014GL062700>, 2014GL062700, 2015.
- Iijima, T. and Potemra, T. A.: The amplitude distribution of field-aligned currents at northern high latitudes observed by Triad, *Journal of Geophysical Research*, 81, 2165–2174, <https://doi.org/10.1029/JA081i013p02165>, <http://dx.doi.org/10.1029/JA081i013p02165>, 1976a.
- Iijima, T. and Potemra, T. A.: Field-aligned currents in the dayside cusp observed by Triad, *Journal of Geophysical Research*, 81, 5971–5979, <https://doi.org/10.1029/JA081i034p05971>, <http://dx.doi.org/10.1029/JA081i034p05971>, 1976b.
- Johansson, T., Marklund, G., Karlsson, T., Liléo, S., Lindqvist, P.-A., Nilsson, H., and Buchert, S.: Scale sizes of intense auroral electric fields observed by Cluster, *Annales Geophysicae*, 25, 2413–2425, <https://doi.org/10.5194/angeo-25-2413-2007>, <http://www.ann-geophys.net/25/2413/2007/>, 2007.
- Juusola, L., Kauristie, K., Vanhamäki, H., Aikio, A., and van de Kamp, M.: Comparison of auroral ionospheric and field-aligned currents derived from Swarm and ground magnetic field measurements, *Journal of Geophysical Research: Space Physics*, 121, 9256–9283, <https://doi.org/10.1002/2016JA022961>, <http://dx.doi.org/10.1002/2016JA022961>, 2016JA022961, 2016.
- Karlsson, T. and Marklund, G. T.: A statistical study of intense low-altitude electric fields observed by Freja, *Geophysical Research Letters*, 23, 1005–1008, <https://doi.org/10.1029/96GL00773>, <http://dx.doi.org/10.1029/96GL00773>, 1996.
- Knudsen, D. J., Donovan, E. F., Cogger, L. L., Jackel, B., and Shaw, W. D.: Width and structure of mesoscale optical auroral arcs, *Geophysical Research Letters*, 28, 705–708, <https://doi.org/10.1029/2000GL011969>, <http://dx.doi.org/10.1029/2000GL011969>, 2001.
- Lühr, H., Warnecke, J., Zanetti, L. J., Lindqvist, P. A., and Hughes, T. J.: Fine structure of field-aligned current sheets deduced from spacecraft and ground-based observations: Initial FREJA results, *Geophysical Research Letters*, 21, 1883–1886, <https://doi.org/10.1029/94GL01278>, <http://dx.doi.org/10.1029/94GL01278>, 1994.
- Lühr, H., Warnecke, J. F., and Rother, M. K. A.: An algorithm for estimating field-aligned currents from single spacecraft magnetic field measurements: a diagnostic tool applied to Freja satellite data, *IEEE Transactions on Geoscience and Remote Sensing*, 34, 1369–1376, <https://doi.org/10.1109/36.544560>, 1996.
- Lühr, H., Park, J., Gjerloev, J. W., Rauberg, J., Michaelis, I., Merayo, J. M. G., and Brauer, P.: Field-aligned currents' scale analysis performed with the Swarm constellation, *Geophysical Research Letters*, 42, 1–8, <https://doi.org/10.1002/2014GL062453>, <http://dx.doi.org/10.1002/2014GL062453>, 2015.
- Lühr, H., Huang, T., Wing, S., Kervalishvili, G., Rauberg, J., and Korth, H.: Filamentary field-aligned currents at the polar cap region during northward interplanetary magnetic field derived with the Swarm constellation, *Annales Geophysicae*, 34, 901–915, <https://doi.org/10.5194/angeo-34-901-2016>, <https://www.ann-geophys.net/34/901/2016/>, 2016.
- Maggs, J. and Davis, T.: Measurements of the thicknesses of auroral structures, *Planetary and Space Science*, 16, 205–209, [https://doi.org/http://dx.doi.org/10.1016/0032-0633\(68\)90069-X](https://doi.org/http://dx.doi.org/10.1016/0032-0633(68)90069-X), <http://www.sciencedirect.com/science/article/pii/003206336890069X>, 1968.
- Maus, S., Rother, M., Stolle, C., Mai, W., Choi, S., Lühr, H., Cooke, D., and Roth, C.: Third generation of the Potsdam Magnetic Model of the Earth (POMME), *Geochemistry, Geophysics, Geosystems*, 7, <https://doi.org/10.1029/2006GC001269>, <http://dx.doi.org/10.1029/2006GC001269>, 2006.



- Maus, S., Manoj, C., Rauberg, J., Michaelis, I., and Lühr, H.: NOAA/NGDC candidate models for the 11th generation International Geomagnetic Reference Field and the concurrent release of the 6th generation Pomme magnetic model, *Earth, Planets and Space*, 62, 2, <https://doi.org/10.5047/eps.2010.07.006>, <http://dx.doi.org/10.5047/eps.2010.07.006>, 2010.
- Mende, S. B., Harris, S. E., Frey, H. U., Angelopoulos, V., Russell, C. T., Donovan, E., Jackel, B., Greffen, M., and Peticolas, L. M.: The THEMIS Array of Ground based Observatories for the Study of Auroral Substorms, pp. 357–387, Springer New York, New York, NY, [https://doi.org/10.1007/978-0-387-89820-9\\_16](https://doi.org/10.1007/978-0-387-89820-9_16), [http://dx.doi.org/10.1007/978-0-387-89820-9\\_16](http://dx.doi.org/10.1007/978-0-387-89820-9_16), 2009.
- Olsen, N., Lühr, H., Finlay, C. C., and Tøffner-Clausen, L.: The CHAOS-4 geomagnetic field model, *Geophys J Int*, 1997, <https://doi.org/10.1093/gji/ggu033>, <http://dx.doi.org/10.1093/gji/ggu033>, 2014.
- Partamies, N., Donovan, E., and Knudsen, D.: Statistical study of inverted-V structures in FAST data, *Annales Geophysicae*, 26, 1439–1449, <https://doi.org/10.5194/angeo-26-1439-2008>, <http://www.ann-geophys.net/26/1439/2008/>, 2008.
- Partamies, N., Syrjäsoo, M., Donovan, E., Connors, M., Charrois, D., Knudsen, D., and Kryzanowsky, Z.: Observations of the auroral width spectrum at kilometre-scale size, *Annales Geophysicae*, 28, 711–718, <https://doi.org/10.5194/angeo-28-711-2010>, <http://www.ann-geophys.net/28/711/2010/>, 2010.
- Ritter, P. and Lühr, H.: Curl-B technique applied to Swarm constellation for determining field-aligned currents, *Earth, Planets and Space*, 58, 463–476, <https://doi.org/10.1186/BF03351942>, <https://doi.org/10.1186/BF03351942>, 2006.
- Ritter, P., Lühr, H., and Rauberg, J.: Determining field-aligned currents with the Swarm constellation mission, *Earth, Planets and Space*, 65, 9, <https://doi.org/10.5047/eps.2013.09.006>, <https://doi.org/10.5047/eps.2013.09.006>, 2013.
- Sonnerup, B. U. O. and Cahill, L. J.: Magnetopause structure and attitude from Explorer 12 observations, *Journal of Geophysical Research*, 72, 171–183, <https://doi.org/10.1029/JZ072i001p00171>, <http://dx.doi.org/10.1029/JZ072i001p00171>, 1967.
- Sonnerup, B. U. Ö. and Scheible, M.: Minimum and Maximum Variance Analysis, in: *Analysis Methods for Multi-spacecraft Data*, edited by Paschmann, G. and Daly, P. W., vol. 1, pp. 185–220, Eur. Space Agency Spec. Publ., ESA SP-449, Hanover, N. H., 1998.
- Stenbaek-Nielsen, H. C., Hallinan, T. J., Osborne, D. L., Kimball, J., Chaston, C., McFadden, J., Delory, G., Temerin, M., and Carlson, C. W.: Aircraft observations conjugate to FAST: Auroral arc thicknesses, *Geophysical Research Letters*, 25, 2073–2076, <https://doi.org/10.1029/98GL01058>, <http://dx.doi.org/10.1029/98GL01058>, 1998.
- Torrence, C. and Compo, G. P.: A Practical Guide to Wavelet Analysis, *Bulletin of the American Meteorological Society*, 79, 61–78, 1998.
- Trondsen, T. S. and Cogger, L. L.: High-resolution television observations of black aurora, *Journal of Geophysical Research: Space Physics*, 102, 363–378, <https://doi.org/10.1029/96JA03106>, <http://dx.doi.org/10.1029/96JA03106>, 1997.
- Tsyganenko, N. A. and Sitnov, M. I.: Modeling the dynamics of the inner magnetosphere during strong geomagnetic storms, *Journal of Geophysical Research: Space Physics*, 110, <https://doi.org/10.1029/2004JA010798>, <http://dx.doi.org/10.1029/2004JA010798>, 2005.
- Vogt, J.: Alfvén wave coupling in the auroral current circuit, *Surveys in Geophysics*, 23, 335–377, <https://doi.org/10.1023/A:1015597724324>, <http://dx.doi.org/10.1023/A:1015597724324>, 2002.
- Vogt, J. and Haerendel, G.: Reflection and transmission of Alfvén waves at the auroral acceleration region, *Geophysical Research Letters*, 25, 277–280, <https://doi.org/10.1029/97GL53714>, <http://dx.doi.org/10.1029/97GL53714>, 1998.
- Vogt, J., Albert, A., and Marghitsu, O.: Analysis of three-spacecraft data using planar reciprocal vectors: methodological framework and spatial gradient estimation, *Annales Geophysicae*, 27, 3249–3273, <https://doi.org/10.5194/angeo-27-3249-2009>, <https://www.ann-geophys.net/27/3249/2009/>, 2009.
- Vogt, J., Sorbalo, E., He, M., and Blagau, A.: Gradient estimation using configurations of two or three spacecraft, *Annales Geophysicae*, 31, 1913–1927, <https://doi.org/10.5194/angeo-31-1913-2013>, <https://www.ann-geophys.net/31/1913/2013/>, 2013.



Wu, J., Knudsen, D. J., Gillies, D. M., Donovan, E. F., and Burchill, J. K.: Swarm Observation of Field-Aligned Currents Associated With Multiple Auroral Arc Systems, *Journal of Geophysical Research: Space Physics*, pp. n/a–n/a, <https://doi.org/10.1002/2017JA024439>, <http://dx.doi.org/10.1002/2017JA024439>, 2017JA024439, 2017.

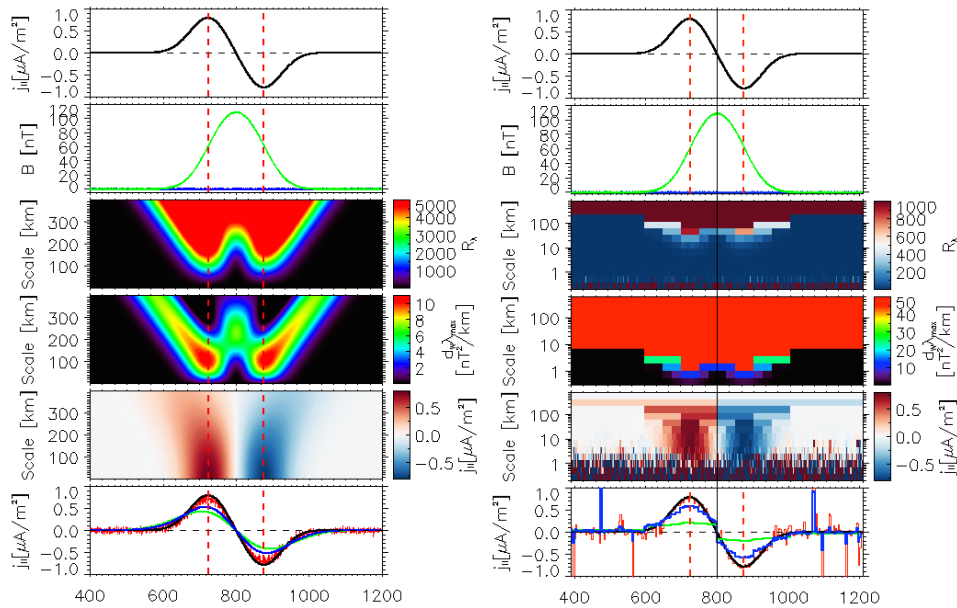


**Figure 1.** MSMVA analysis for the linear (left) and logarithmic scheme (right). Left: a1) Input FAC density; b1) Magnetic field perturbation; c1) Planarity,  $R_\lambda$ ; d1) FAC scale/location,  $\partial_w \lambda_\gamma$ ; e1) Multiscale FAC density; (f1) AW (blue), SW (red), LW (green) compared with the input FAC density (black). Right: Same quantities as in left panels for the logarithmic scheme.

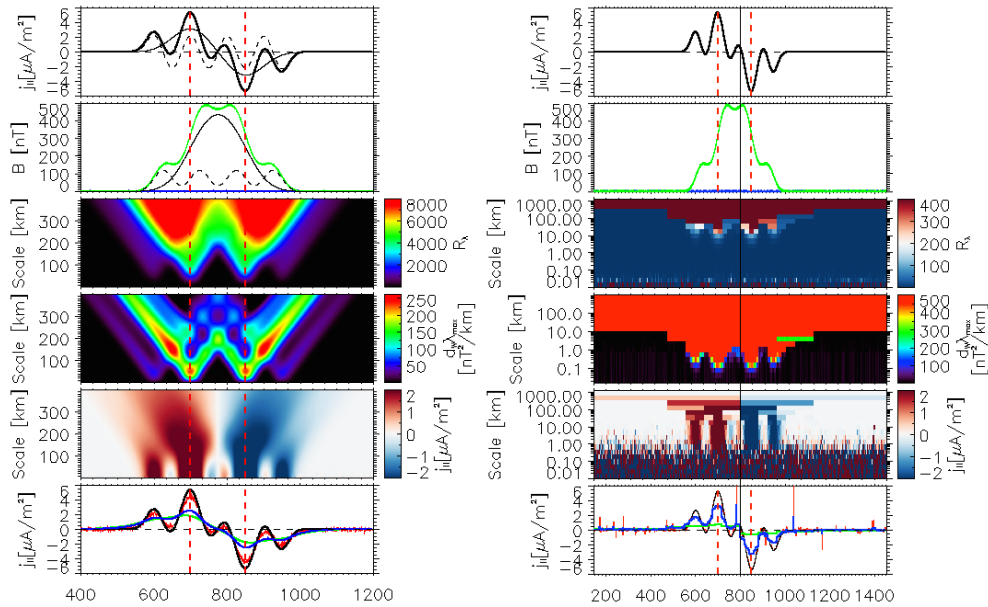


**Figure 2.** MSMVA analysis for the linear (left) and logarithmic scheme (right). Left: a1) Input FAC density; b1) Magnetic field perturbation; c1) Planarity,  $R_\lambda$ ; d1) FAC scale/location,  $\partial_w \lambda_\eta$ ; e1) Multiscale FAC density; (f1) AW (blue), SW (red), LW (green) compared with the input FAC density (black). Right: Same quantities as in left panels for the logarithmic scheme.

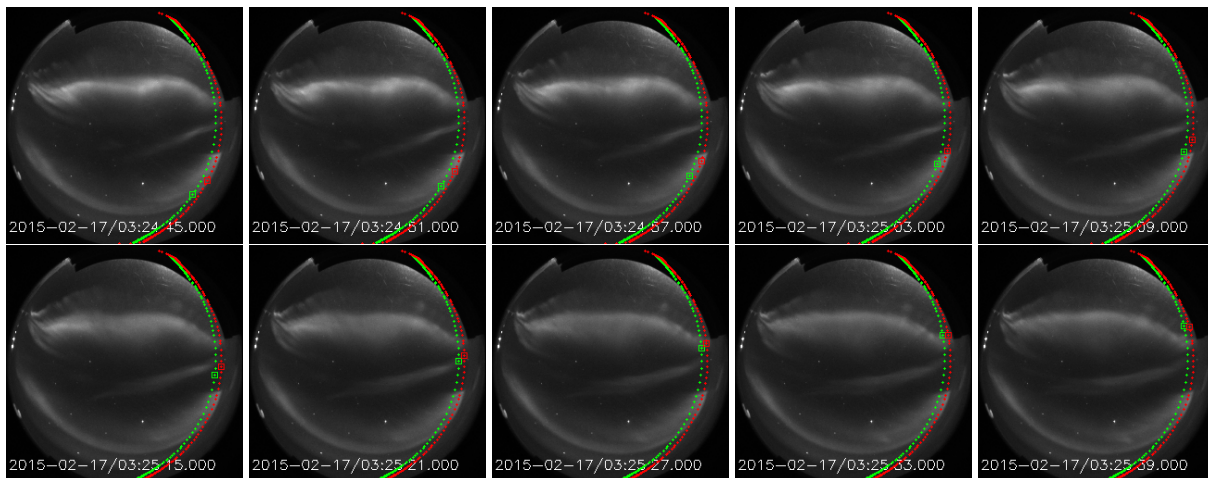


**Figure 3.** Optical frames in the instrument coordinate from SNKQ station. The tracks show the ionospheric projection of SwA (green) and SwC (red). At the time of the frame the spacecraft mapped position is shown by the square symbols. The time is overlaid on each frame and covers the interval from 03:24:45 to 03:25:39.

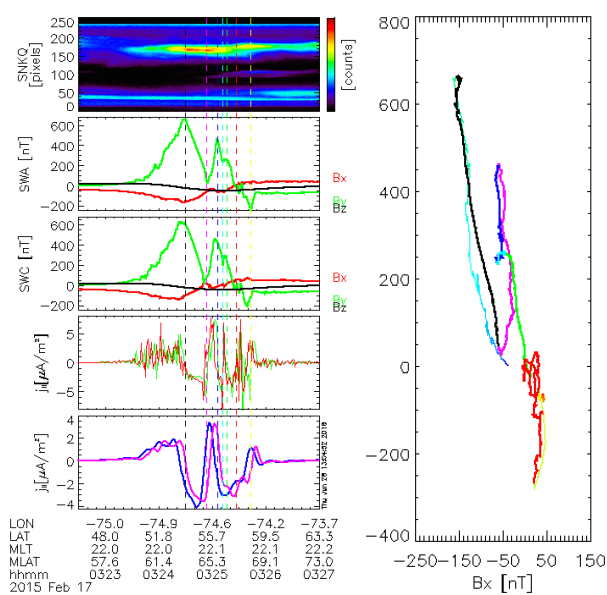


**Figure 4.** Left: a) Keogram from SNQ station; b-c) Magnetic field perturbation from SwA and SwC. d) FAC density estimated by the FD method (L2 product) on SwA (green) and SwC (red); e) The FAC density estimates based on the two-spacecraft FD (magenta) and LS (blue) method, respectively. The vertical dashed lines indicate the beginning of various FAC elements. Right: Hodogram representation of  $B_{\perp}$ . For each FAC segment we use the same color used in the left panels to indicate the beginning of the respective FAC element.

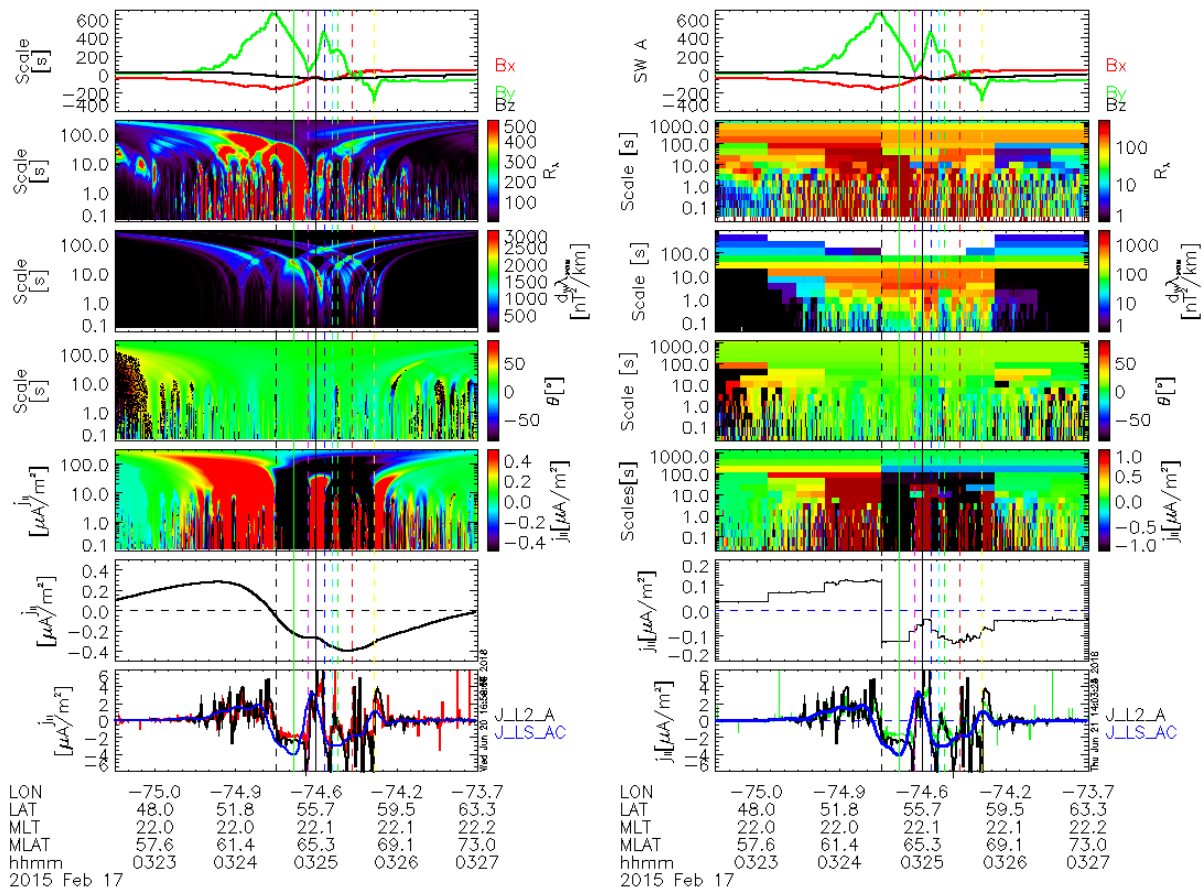


**Figure 5.** MSMVA analysis for the linear (left) and logarithmic (right) scheme. Left: a) Magnetic field perturbation; b) Planarity  $R_\lambda$ ; c) FAC location and characteristic scale  $\partial_\omega \lambda_\eta$ ; d) Orientation; e) Multiscale FAC density; (f) LW (black); (g-h) Single-spacecraft FD (black), two-spacecraft LS (blue), SW (red). Right: Same panels for the logarithmic scale sampling with the difference that panel g shows AW (green) estimate. The vertical solid lines indicate the times for which we show the sections in Figure 6.

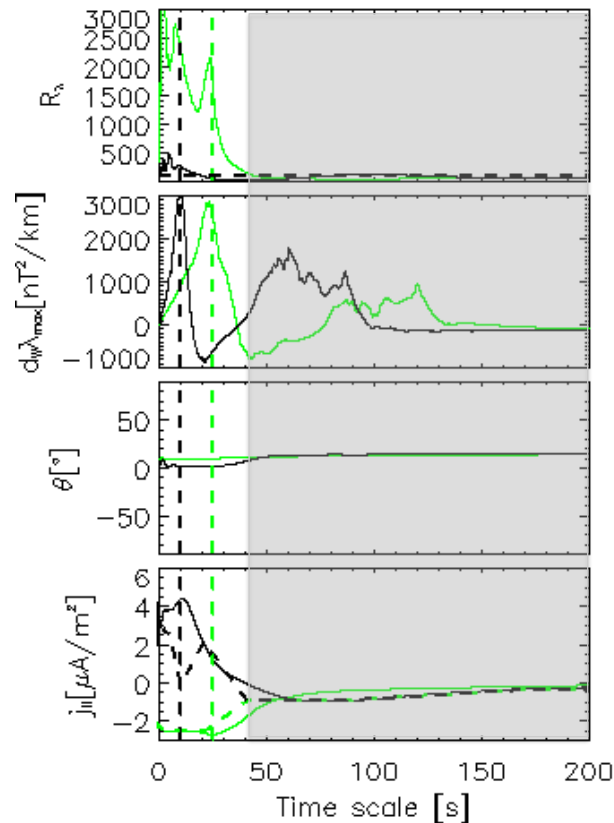


**Figure 6.** Sections in the MSMVA spectra. a)  $R_\lambda$ ; b)  $\partial_w \lambda_\eta$ ; c)  $\theta$ ; d)  $j_{||}$  inferred by the linear (solid line) and the logarithmic (dashed line) scale sampling scheme. The profiles are taken in the middle of the upward and downward FACs located at 03:24:43 and 03:25:00, respectively. These times are indicated by the vertical solid lines in Figure 5. The horizontal dash line in (a) indicate reference level  $R_\lambda=100$  discussed in the text. The marked gray area indicates the region where  $R_\lambda < 100$  for the selected sections.

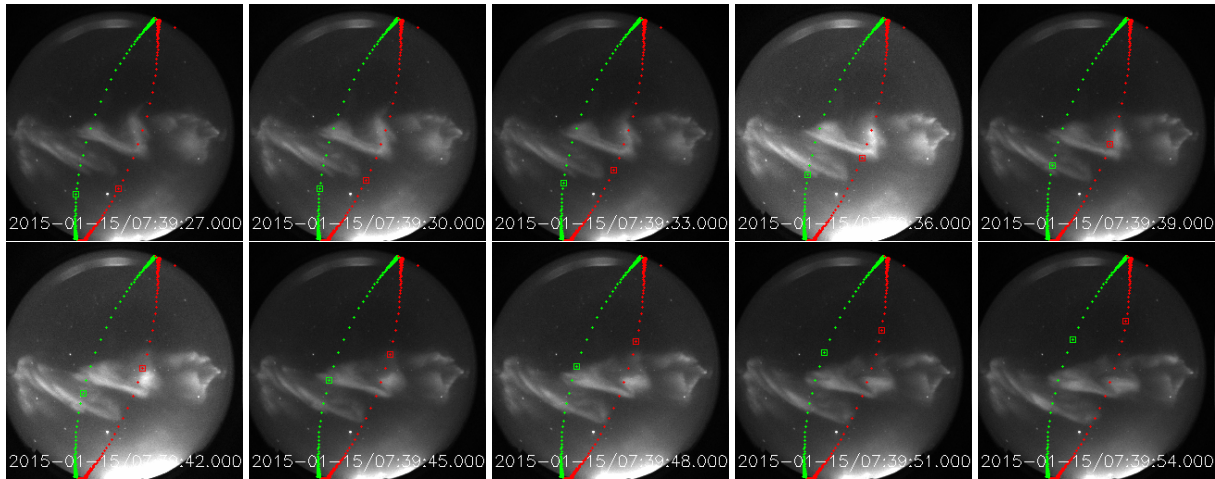


**Figure 7.** Optical frames in the instrument coordinate from RANK station. The tracks show the ionospheric projection of SwA (green) and SwC (red). At the time of the frame the spacecraft mapped position is shown by the square symbols. The time is overplotted on each frame and covers the interval from 07:39:27 to 07:39:54.

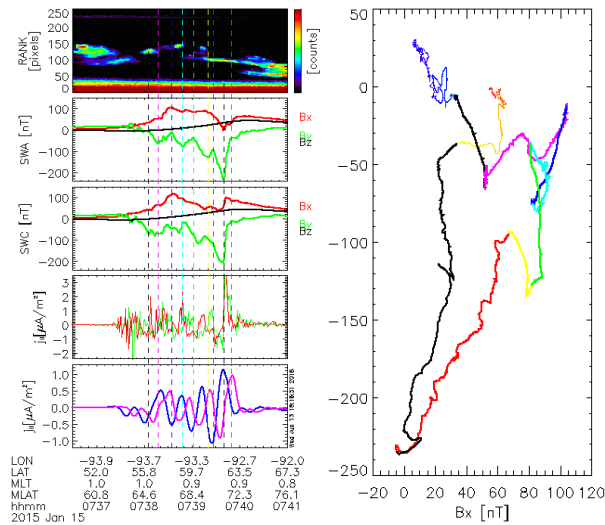


**Figure 8.** Left: a) Keogram from RANK station; b-c) Magnetic field perturbation from SwA and SwC. d) FAC density estimated by the FD method (L2 product) on SwA (green) and SwC (red); e) The FAC density estimates based on the two-spacecraft FD (magenta) and LS (blue) method, respectively. The vertical dashed lines indicate the beginning of various FAC elements. Right: Hodogram representation of  $B_{\perp}$ . For each FAC segment we use the same color used in the left panels to indicate the beginning of the respective FAC element.

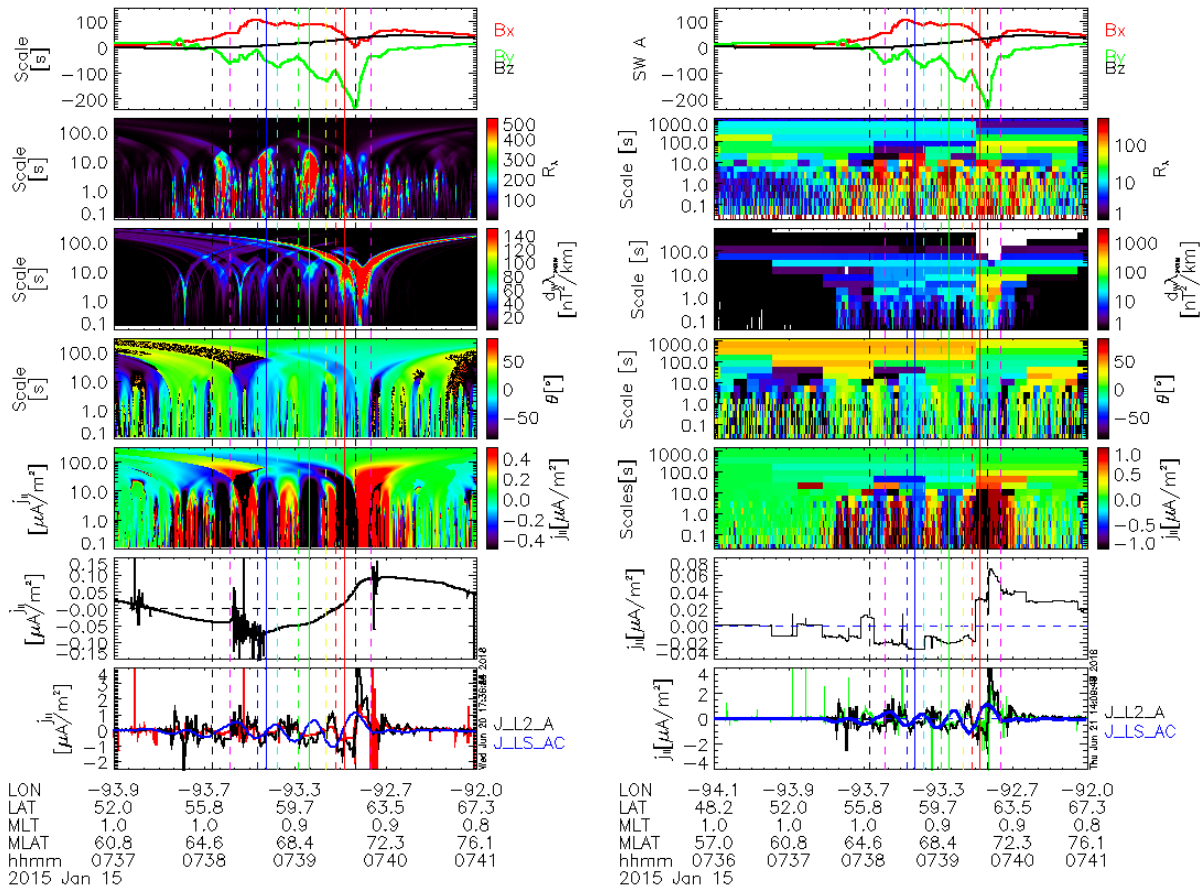


**Figure 9.** MSMVA analysis for the linear (left) and logarithmic (right) scheme. Left: a) Magnetic field perturbation; b) Planarity  $R_\lambda$ ; c) FAC location and characteristic scale  $\partial_\omega \lambda_n$ ; d) Orientation; e) Multiscale FAC density; (f) LW (black); (g-h) Single-spacecraft FD (black), two-spacecraft LS (blue), SW (red). Right: Same panels for the logarithmic scale sampling with the difference that panel g shows AW (green) estimate. The vertical solid lines indicate the times for which we show the sections in Figure 10.

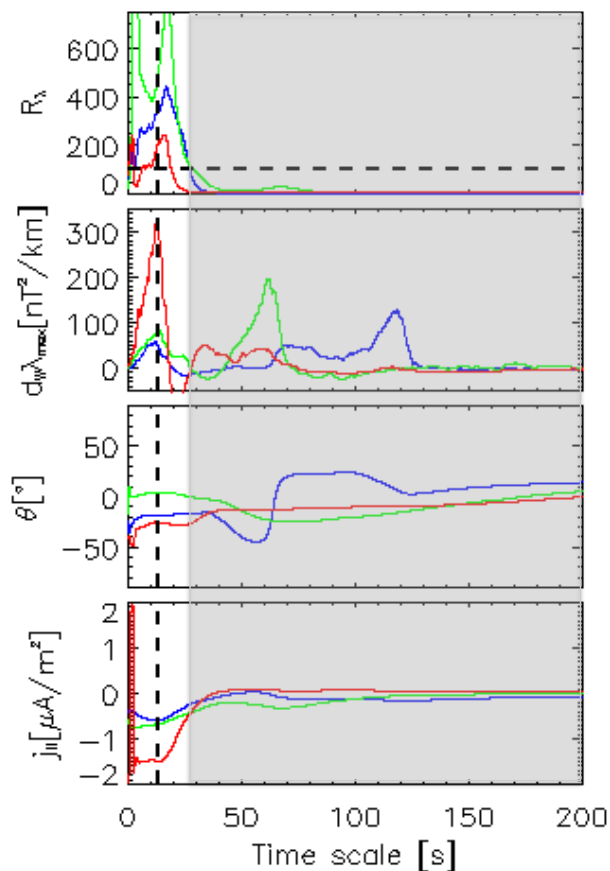


**Figure 10.** Sections in the MSMVA spectra. a)  $R_\lambda$ ; b)  $\partial_w \lambda_\eta$ ; c)  $\theta$ ; d)  $j_{||}$  inferred by the linear (solid line) scale sampling scheme. The profiles are taken in the middle of the upward FACs located at 07:38:41 (blue) and 07:39:09 (green), and 07:39:33 (red). These times are indicated by the vertical solid lines in Figure 9. The horizontal dash line in (a) indicate reference level  $R_\lambda=100$  discussed in the text. The marked gray area indicates the region where  $R_\lambda < 100$  for the selected sections.

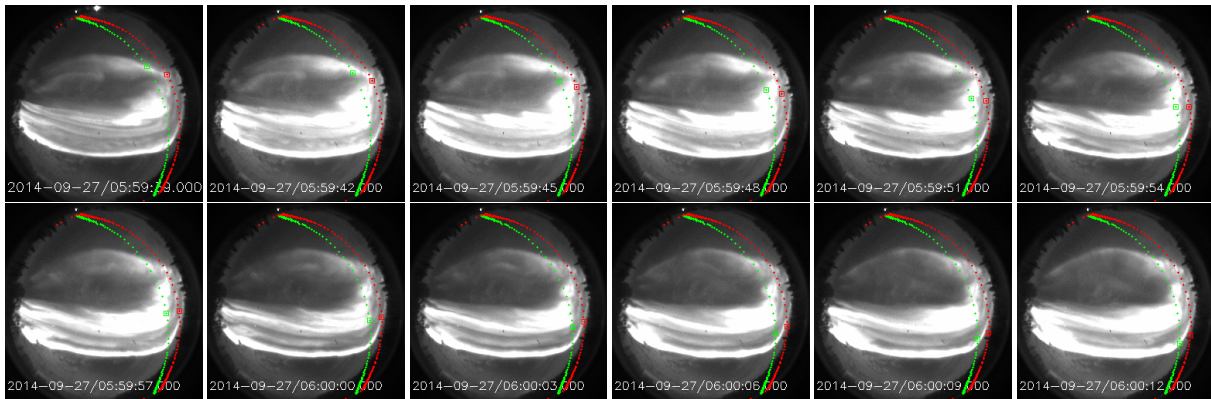


**Figure 11.** Optical frames in the instrument coordinate from FSMI station. The tracks show the ionospheric projection of SwA (green) and SwC (red). At the time of the frame the spacecraft mapped position is shown by the square symbols. The time is overplotted on each frame and covers the interval from 05:59:39 to 06:00:12.

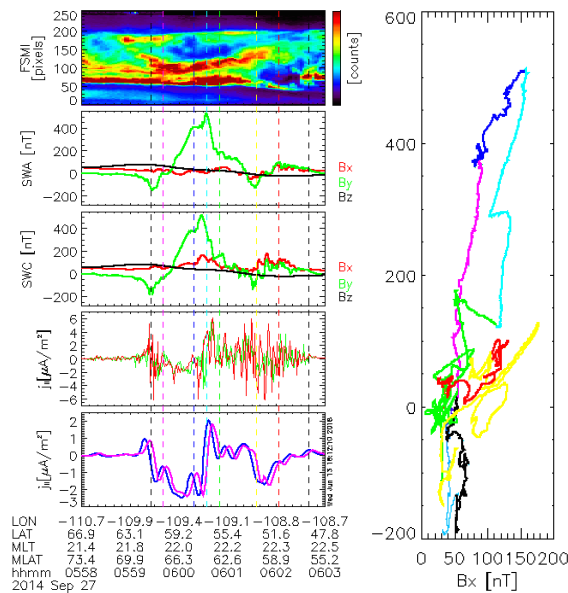


**Figure 12.** Left: a) Keogram from FSMI station; b-c) Magnetic field perturbation from SwA and SwC. d) FAC density estimated by the FD method (L2 product) on SwA (green) and SwC (red); e) The FAC density estimates based on the two-spacecraft FD (magenta) and LS (blue) method, respectively. The vertical dashed lines indicate the beginning of various FAC elements. Right: Hodogram representation of  $B_{\perp}$ . For each FAC segment we use the same color used in the left panels to indicate the beginning of the respective FAC element.

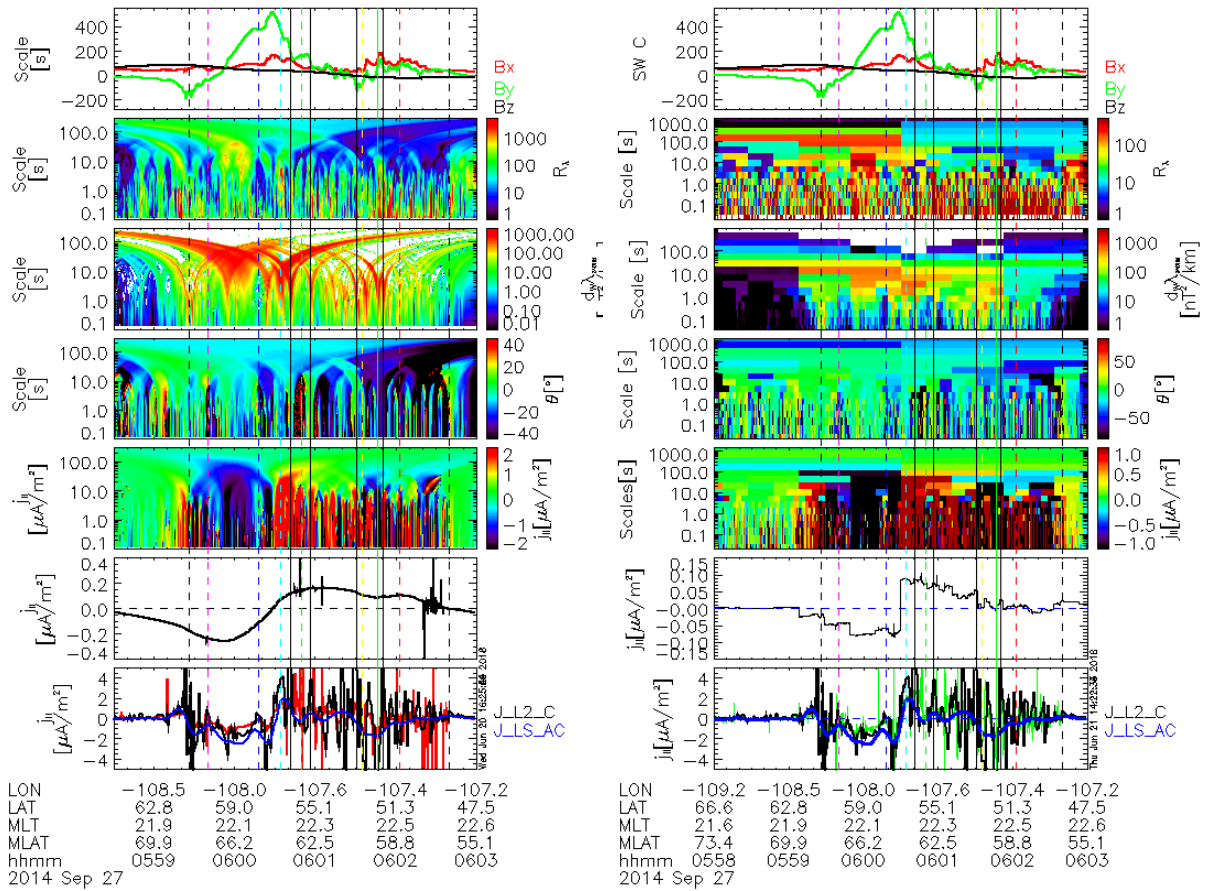


**Figure 13.** MSMVA analysis for the linear (left) and logarithmic (right) scheme. Left: a) Magnetic field perturbation; b) Planarity  $R_\lambda$ ; c) FAC location and characteristic scale  $\partial_w \lambda_\eta$ ; d) Orientation; e) Multiscale FAC density; (f) LW (black); (g) Single-spacecraft FD (black), two-spacecraft LS (blue), SW (red). Right: Same panels for the logarithmic scale sampling with the difference that panel g shows AW (green) estimate. The vertical solid lines indicate the times for which we show the sections in Figure 14.

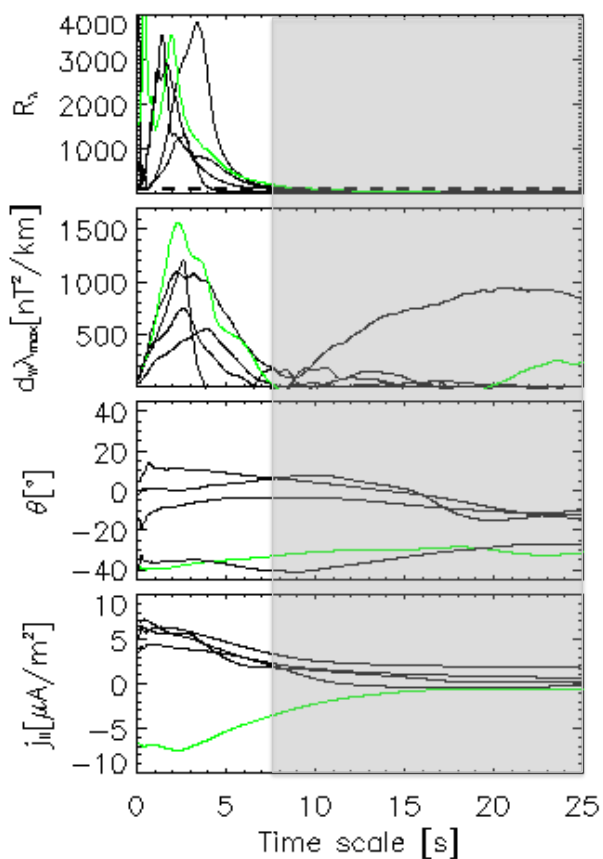


**Figure 14.** Sections in the MSMVA spectra. a)  $R_\lambda$ ; b)  $\partial_w \lambda_\eta$ ; c)  $\theta$ ; d)  $j_{||}$  inferred by the linear (solid line) scale sampling scheme. The profiles are taken at the times indicated by the solid vertical lines in Figure 13. The horizontal dash line in (a) indicate reference level  $R_\lambda=100$  discussed in the text. The marked gray area indicates the region where  $R_\lambda < 100$  for the selected sections.